



Upwelling in the Alaskan Beaufort Sea: Atmospheric forcing and local versus non-local response

Robert S. Pickart^{a,*}, Michael A. Spall^a, G.W.K. Moore^b, Thomas J. Weingartner^c, Rebecca A. Woodgate^d, Knut Aagaard^d, Koji Shimada^e

^a Woods Hole Oceanographic Institution, Woods Hole, MA 02540, USA

^b University of Toronto, Toronto, ON, Canada M5S 1A1

^c University of Alaska, Fairbanks; Fairbanks, AK 99775, USA

^d Applied Physics Laboratory, University of Washington, Seattle, WA 98105-6698, USA

^e Japan Agency for Marine-Earth Science and Technology, Yokosuka 237-0061, Japan

ARTICLE INFO

Article history:

Received 8 March 2010

Received in revised form 24 November 2010

Accepted 25 November 2010

Available online 24 December 2010

ABSTRACT

The spin up and relaxation of an autumn upwelling event on the Beaufort slope is investigated using a combination of oceanic and atmospheric data and numerical models. The event occurred in November 2002 and was driven by an Aleutian low storm. The wind field was strongly influenced by the pack-ice distribution, resulting in enhanced winds over the open water of the Chukchi Sea. Flow distortion due to the Brooks mountain range was also evident. Mooring observations east of Barrow Canyon show that the Beaufort shelfbreak jet reversed to the west under strong easterly winds, followed by upwelling of Atlantic Water onto the shelf. After the winds subsided a deep eastward jet of Atlantic Water developed, centered at 250 m depth. An idealized numerical model reproduces these results and suggests that the oceanic response to the local winds is modulated by a propagating signal from the western edge of the storm. The disparity in wave speeds between the sea surface height signal—traveling at the fast barotropic shelf wave speed—versus the interior density signal—traveling at the slow baroclinic wave speed—leads to the deep eastward jet. The broad-scale response to the storm over the Chukchi Sea is investigated using a regional numerical model. The strong gradient in windspeed at the ice edge results in convergence of the offshore Ekman transport, leading to the establishment of an anti-cyclonic gyre in the northern Chukchi Sea. Accordingly, the Chukchi shelfbreak jet accelerates to the east into the wind during the storm, and no upwelling occurs west of Barrow Canyon. Hence the storm response is fundamentally different on the Beaufort slope (upwelling) versus the Chukchi slope (no upwelling). The regional numerical model results are supported by additional mooring data in the Chukchi Sea.

© 2010 Elsevier Ltd. All rights reserved.

1. Introduction

It is now well-established that a shelfbreak current carrying Pacific-origin water exists at the edge of the Chukchi and Alaskan Beaufort Seas (Pickart et al., 2004; Mathis et al., 2007; Spall et al., 2008; Nikolopoulos et al., 2009). The current is narrow (order 15–20 km) and, in the absence of wind-forcing, flows to the east towards the Canadian Arctic Archipelago. One of the important aspects of this current is that it dynamically impacts the exchange of water between the shelves and the interior basin of the western Arctic. Such exchange is crucial for a wide range of issues and processes, many of them climate-related. For example, it is believed that the halocline of the Canada basin is ventilated laterally from the shelves (e.g. Aagaard et al., 1981; Cavalieri and Martin, 1994;

Shimada et al., 2005) rather than through vertical processes. Also, the flux of warm surface water from the shelf to the basin interior is thought to be partly responsible for the recent decline in sea ice cover (e.g. Shimada et al., 2006; Zhang et al., 2008; Woodgate et al., 2010). Pacific-origin waters, being rich in nutrients (e.g. Walsh et al., 1989), also impact the productivity of the interior basin and carry a distinct signal of zooplankton to the north (Nelson et al., 2009; Llinás et al., 2009). The recent changes in water properties of the Pacific water inflow through Bering Strait (Woodgate et al., 2006, 2010) will likely have profound impacts on the physical structure and ecosystem of the western Arctic (e.g. Carmack and Wassmann, 2006). However, for us to understand and ultimately predict this response, we must first understand the nature and dynamics of the shelf-basin exchange, which, to first order, involves the shelfbreak current.

Two primary mechanisms of shelf-basin exchange across the shelfbreak jet are hydrodynamic instability of the current, leading to eddy formation, and wind-induced exchange, leading to

* Corresponding author.

E-mail address: rpickart@whoi.edu (R.S. Pickart).

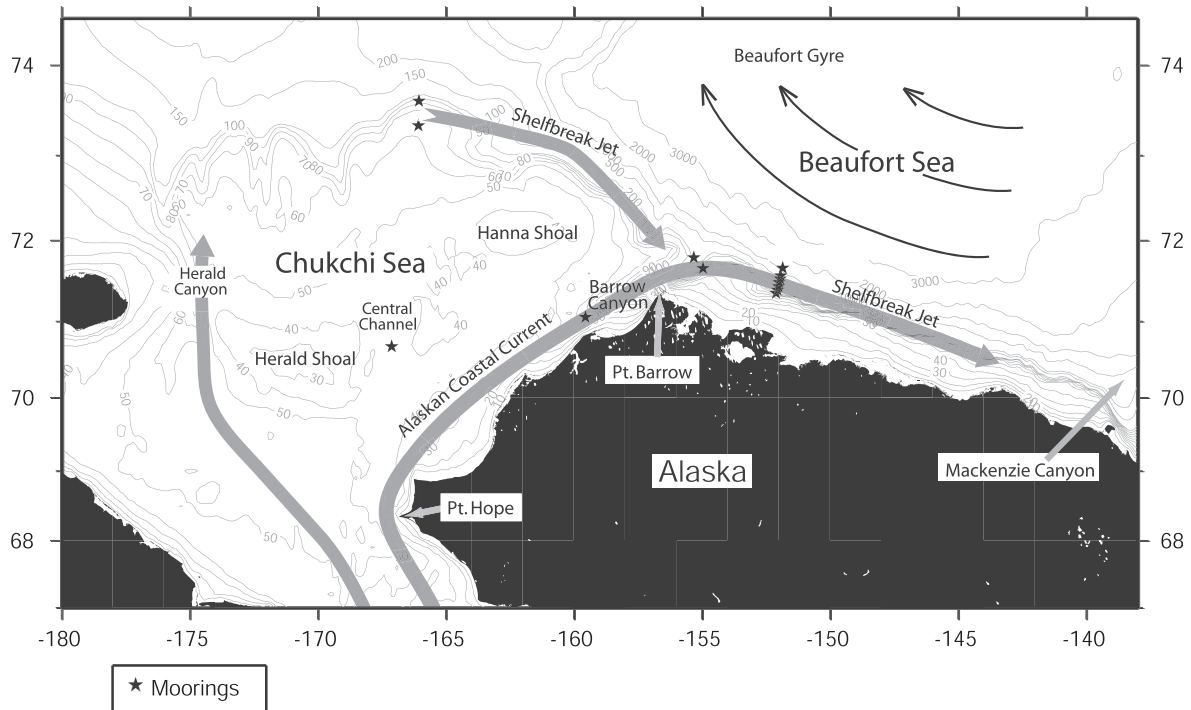


Fig. 1. Schematic circulation of the Chukchi and Beaufort Seas (after Spall et al. (2008)). The locations of the moorings used in the study are indicated by the stars, and the weather station is located at Pt. Barrow. The bathymetric contours are 10–100 m by 10 m increments, 150 m, 200 m, 500 m, 1000 m, 2000 m, and 3000 m.

upwelling or downwelling. The Canada basin is thought to contain a large number of anti-cyclonic, Pacific Water eddies (e.g. Manley and Hunkins, 1985; Muench et al., 2000; Mathis et al., 2007). It has been demonstrated that one of the formation mechanisms of the eddies is baroclinic instability of the boundary current. This happens near the abrupt topography of Barrow Canyon (Fig. 1; e.g. Chao and Shaw, 2003; Pickart et al., 2005; Pickart and Stossmeister, 2008; Watanabe and Hasumi, 2009), and also occurs in regions of “well behaved” topography, i.e. along the shelfbreak (Spall et al., 2008). Both warm and cold eddies are expelled by the jet, which impact the ventilation and stratification of the interior as well as the nutrient distribution of the Canada Basin (Mathis et al., 2007).

Wind-driven exchange also occurs along the continental shelf and slope of the Chukchi and Beaufort Seas. Although downwelling takes place (e.g. Melling, 1993), upwelling events are more prevalent, usually due to easterly or northeasterly winds associated with Aleutian low storms located to the south (Pickart et al., 2009b). Much of the upwelling observed to date is associated with anomalous topography, e.g. at Barrow Canyon (Aagaard and Roach, 1990), Mackenzie Canyon (Carmack and Kulikov, 1998), and within smaller canyons along the Beaufort shelf (Williams et al., 2008). The primary signature of such events is the appearance of warm and salty Atlantic Water at shallow depths.¹ At Barrow Canyon, strong up-canyon flows can advect Atlantic Water well onto the Chukchi shelf (Aagaard and Roach, 1990; Bourke and Paquette, 1976). Upwelling occurs along the shelfbreak as well, away from canyons (Woodgate et al., 2005a; Nikolopoulos et al., 2009). Nikolopoulos et al. (2009) found that the dominant autumn and wintertime velocity variability observed in mooring records along the Alaskan Beaufort slope was due to flow reversals associated with upwelling. Indeed, during the four-month period from October 2002–January

2003, 18 upwelling events were observed (Pickart et al., 2009b). Similar events have been measured away from canyons in the Canadian Beaufort Sea as well (Carmack and Kulikov, 1998).

Despite the prevalence of upwelling along the southern edge of the Canada Basin, there is much we don’t know about the nature of these events, including the atmospheric forcing, the dynamics of the water column response, the impact of sea ice (both land-fast and pack-ice), and the magnitude of the resulting cross-stream fluxes of mass and other properties. While Atlantic Water is drawn onto the shelf, the dynamics of both the primary (alongstream) and secondary (cross-stream) circulations remain unclear. Particularly little is known about the offshore flux of near-surface water during upwelling because of the dearth of shallow measurements (due to the ice cover). Yang (2006) argues that the wind-driven, offshore fluxes of heat and freshwater in the upper layer contribute significantly to the Beaufort Gyre. The relative role of local versus remote winds in driving the upwelling is also uncertain. Both Aagaard and Roach (1990) and Carmack and Kulikov (1998) present evidence for eastward propagation of upwelling signals due to shelf-edge or Kelvin waves. In fact, Aagaard and Roach (1990) found little correlation between mooring records in Barrow Canyon and the local wind field. On the other hand, Pickart et al. (2009b) found a strong relationship between the occurrence of upwelling on the Alaskan Beaufort slope and the measured winds at the nearby Pt. Barrow meteorological station.

To date there has been limited numerical modeling addressing upwelling in the western Arctic. Chapman and Carmack (2003) investigated the role of ice cover in dictating the nature of the response, using an idealized numerical model wherein the ice cover was immovable (i.e. impenetrable to the wind). They found fundamentally different circulations depending on whether or not the summertime ice edge was located shoreward or seaward of the shelfbreak. In the latter case, strong upwelling occurred at the shelfbreak, whereas in the former case the circulation was limited to the shelf with no cross-slope exchange. Williams and Carmack (2010) studied upwelling in a two-dimensional framework,

¹ More precisely, the upwelled water is from the upper part of the mid-depth Atlantic Water layer, often referred to as lower halocline Atlantic Water. For the purposes of this paper we will simply refer to the water as Atlantic Water.

configured for the Canadian Beaufort shelf and slope. Under the influence of easterly wind stress, a westward-flowing, bottom-intensified shelfbreak jet developed, with strong cross-stream flow in the surface (offshore flow) and bottom (onshore flow) boundary layers. This response is similar to earlier studies of upwelling at mid-latitudes (e.g. Lentz and Chapman, 2004). Many previous studies (both modeling and observational) have addressed upwelling along the northern California shelf (e.g. Lentz, 1987), the results of which have bearing on the Arctic system. One aspect of note on the California shelf is the occurrence of poleward relaxation flows (i.e. in the opposite direction to the wind) after the cessation of the upwelling winds (e.g. Send et al., 1987; Lentz, 1987; Pringle and Dever, 2009; Melton et al., 2009). Up until now, no analogous feature has been investigated in the western Arctic Ocean.

In this paper we diagnose an upwelling event in the Alaskan Beaufort Sea using a combination of oceanic and atmospheric data and numerical models. The goal of the work is to increase our understanding of the forcing, kinematics, and dynamics of upwelling in the western Arctic Ocean. This is important in light of the many impacts of shelf-basin exchange at high latitudes noted above, particularly during this time of rapidly changing climatic conditions. We analyze in detail a single storm event that occurred in early November 2002 using data from a high-resolution mooring array and a simplified numerical ocean model. We begin by considering the atmospheric forcing, followed by examination of the water column response. The response is characterized by the reversal of the shelfbreak jet into an intense westward-flowing current, along with a strong secondary circulation that leads to upwelling. Shortly after the end of the storm an eastward-directed relaxation flow develops. The model indicates that both the upwelling and the relaxation flow are three-dimensional in nature. Finally, the larger-scale response to the storm over the broad Chukchi shelf and slope is addressed using a more realistically configured numerical model and additional mooring data.

2. Data and methods

2.1. Mooring data

The primary observational data set used in this study comes from a mooring array that was deployed across the shelfbreak current in the Alaskan Beaufort Sea between August 2002 and September 2004 as part of the Western Arctic Shelf-Basin Interactions (SBI) experiment (Figs. 1 and 2). The configuration of the array, data quality, and measurement accuracies are presented in Nikolopoulos et al. (2009) and Spall et al. (2008). Briefly, the array consisted of a cross-slope line of 7 moorings situated at 152°W, with lateral resolution of 5–7 km (except for the seaward-most mooring spaced roughly 10 km away, Fig. 2). The deformation radius in this region of the Arctic is order 10 km, so the mooring array marginally resolves the relevant lateral scales.

Each mooring contained a conductivity/temperature/depth (CTD) profiler providing vertical traces of hydrographic variables 2–4 times per day (vertical resolution of 2 m) between the seafloor and approximately 45 m depth. Upward-facing acoustic Doppler current profilers (ADCPs) near the bases of the moorings provided hourly vertical profiles of eastward and northward velocities at the five shoreward sites (vertical resolution of 5–10 m). The near-surface blanking interval of the ADCP measurements ranged from a depth of 8 m below the surface at the onshore site (BS2) to 45 m below the surface at site BS6. The profiling acoustic current meter data at the two offshore-most sites (BS7, BS8) are not used in this study. The velocity data were de-tided and put into a rotated coordinate system (described below). The strength of the inertial signal throughout the mooring records was estimated using complex demodulation, and was found to be significantly less than both the primary and secondary mesoscale flows of interest. The hydrographic data were used to construct vertical sections of potential temperature, salinity, and potential density (see Spall et al. (2008)

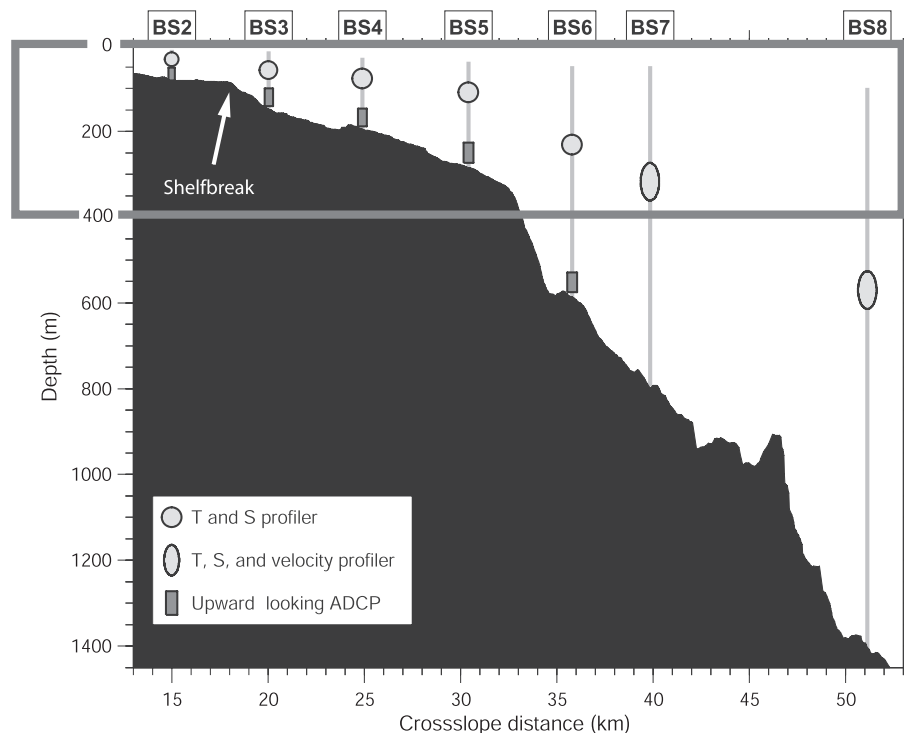


Fig. 2. The SBI Beaufort slope mooring array (from Spall et al., 2008). Mooring names are indicated along the top, and the instrumentation used is listed in the key. The gray rectangle denotes the part of the domain shown in Figs. 9–14. The location of the shelfbreak is marked by the white arrow (corresponding to the 85 m isobath).

for details), and the ADCP data were used to make vertical sections of alongstream and cross-stream velocity (see Nikolopoulos et al. (2009) for details).

To address the large-scale response to the storm, additional mooring data from the SBI experiment were used together with mooring data collected by the Japan Agency for Marine–Earth Science and Technology (JAMSTEC). Two of the SBI moorings were placed on the Chukchi slope near 166°W at a bottom depth of 68 m and 105 m, respectively, for the time period August 2002–September 2004. Both moorings contained upward-facing ADCPs, conventional current meters, and point CTD sensors (see Woodgate et al. (2003) for a discussion). The final two SBI moorings were deployed at the head of Barrow Canyon and in the Central Channel of the Chukchi Sea, respectively (Fig. 1). These contained upward-facing ADCPs and point CTD sensors. Finally, JAMSTEC maintained moorings at the mouth of Barrow Canyon, one on each side of the canyon. All of the additional velocity records were low-passed using a 30-h Butterworth filter to remove the tidal and inertial signals. The combination of these 13 moorings offers a uniquely broad perspective of the Chukchi and Beaufort Seas.

2.2. Meteorological reanalysis fields and forecast models

To investigate the atmospheric forcing we used two different reanalysis products from the National Centers for Environmental Prediction (NCEP). The first is the 6-hourly global product with a spatial resolution of 2.5° for sea-level pressure, and approximately 1.9° for the 10 m winds. It is based on the global data assimilation and forecast model that was operational at NCEP in 1994. This was the product used by Pickart et al. (2009b) to characterize the types of Aleutian low storms that result in upwelling along the Beaufort slope. Here we are more interested in the details of the local wind field, so we also considered a higher resolution NCEP product known as the North American Regional Reanalysis (NARR). This has a temporal resolution of 3 h and spatial resolution of 32 km (Mesinger et al., 2006). It incorporates advances in data assimilation and modeling that have occurred since the original development of the NCEP global reanalysis. In particular, it uses the 2001 operational version of the NCEP ETA model and its 3DVAR data assimilation system that includes direct assimilation of satellite radiances and precipitation, with lateral boundary conditions provided by the NCEP-2 global reanalysis.

For a higher spatial resolution view of the atmospheric flow in the vicinity of the mooring array, we also used the results of two numerical weather prediction models. The first is the operational output from NCEP's ETA model as archived by the Alaska North Slope project. The model output is available on Grid #242 that encompasses our domain of interest and has a temporal resolution of 6 h and spatial resolution of 12 km. The second is the WRF atmospheric model (e.g. Skamarock and Klemp, 2008), which was used to carry out a high resolution simulation of the storm event in question. The model was configured to run in a triple nested configuration with one-way communication using a 60 km resolution outer domain covering the entire North Pacific and Western Arctic, a second domain with 15 km resolution covering the Gulf of Alaska/Chukchi/Beaufort Seas and southern Canada Basin, and a 3.75 km inner domain over the Chukchi and Beaufort Seas and adjacent interior to 75°N. The boundary and initial conditions for the outer domain were obtained from the 6-hourly NCEP Final Analysis, and the simulation was run for 72 h. We note that an additional benefit of the higher resolution models is a more accurate representation of the coastal boundary.

2.3. Meteorological timeseries

Data from the Pt. Barrow weather station were also used in the analysis. The station is located approximately 150 km to the west of the Beaufort slope mooring array (see Fig. 1). While other meteorological stations have been situated to the east of the array (e.g. Barter Island and Prudhoe), these records have been inconsistent and are not as long-term as the Barrow timeseries. The 10 m winds from Pt. Barrow were edited and interpolated as described in Nikolopoulos et al. (2009). Part of our rationale is to assess how good the various meteorological products are in this region of the Arctic, and also assess how representative the Pt. Barrow wind timeseries is for describing the atmospheric forcing at the array site. For the joint analysis with the oceanic data, the wind velocity from the Pt. Barrow meteorological station was converted to windstress following Large and Pond (1981).

3. Synoptic scale overview of the storm

3.1. General features

The extra-tropical cyclone responsible for the winds that resulted in the upwelling event in question propagated across the North Pacific, crossing the International Date Line (180°W) on 2 November 2002 (approximately two and a half days before the winds increased at the array site). The path of the storm is shown in Fig. 3 along with its mean structure during its deepest phase. Its central pressure on 2 November was approximately 990 mb, and as the storm passed south of the Aleutian Island chain on 3 November this dropped slightly to 982 mb. It is often the case that such storms intensify in the area of the island chain (hence the name “Aleutian Low”, e.g. Wilson and Overland, 1986), and this storm was no exception. Over the next 24 h the low underwent an explosive deepening, reaching a central pressure of 957 mb on 4 November. Consistent with the canonical storm evolution in this area discussed by Pickart et al. (2009a), the rapid deepening of the storm was the result of the interaction between an upper-level potential vorticity anomaly and the surface low through the baroclinic growth mechanism discussed by Hoskins et al. (1985).

During the 3-day period of highest winds at the array site (5–7 November), the low moved in a northwesterly direction (Fig. 4). The cyclonic rotation of the low during this period resulted in northwesterly movement of the cold front towards and ultimately over Alaska so that at 0000Z on 6 November, a band of high winds existed along 130°W over the eastern Gulf of Alaska as well as along the north slope (Fig. 4b). A frontal cyclone rapidly developed along this cold front and by 0000Z on 7 November it was located just south of Alaska (Fig. 4c). At this time the parent cyclone was starting to fill, which contributed to the reduction in the sea-level pressure gradient and weakening of the surface winds in the Bering, Chukchi, and Beaufort Seas.

3.2. Small-scale features

We now consider the detailed meteorological conditions in the vicinity of the mooring array. Fig. 5 shows the average 10m wind field in the region of interest over the time period 4–7 November from the four meteorological products: NCEP global (Fig. 5a) and regional (Fig. 5b) reanalysis, as well as the operational ETA model (Fig. 5c) and the WRF research model (Fig. 5d). The dominant feature of the wind field is the enhanced surface flow over the Chukchi and western Beaufort Seas, which is captured in all of the products. Note the turning of the wind from an easterly orientation along the north slope to northeasterly over the central Chukchi Sea. As presented in Pickart et al. (2009b), this general distribution of

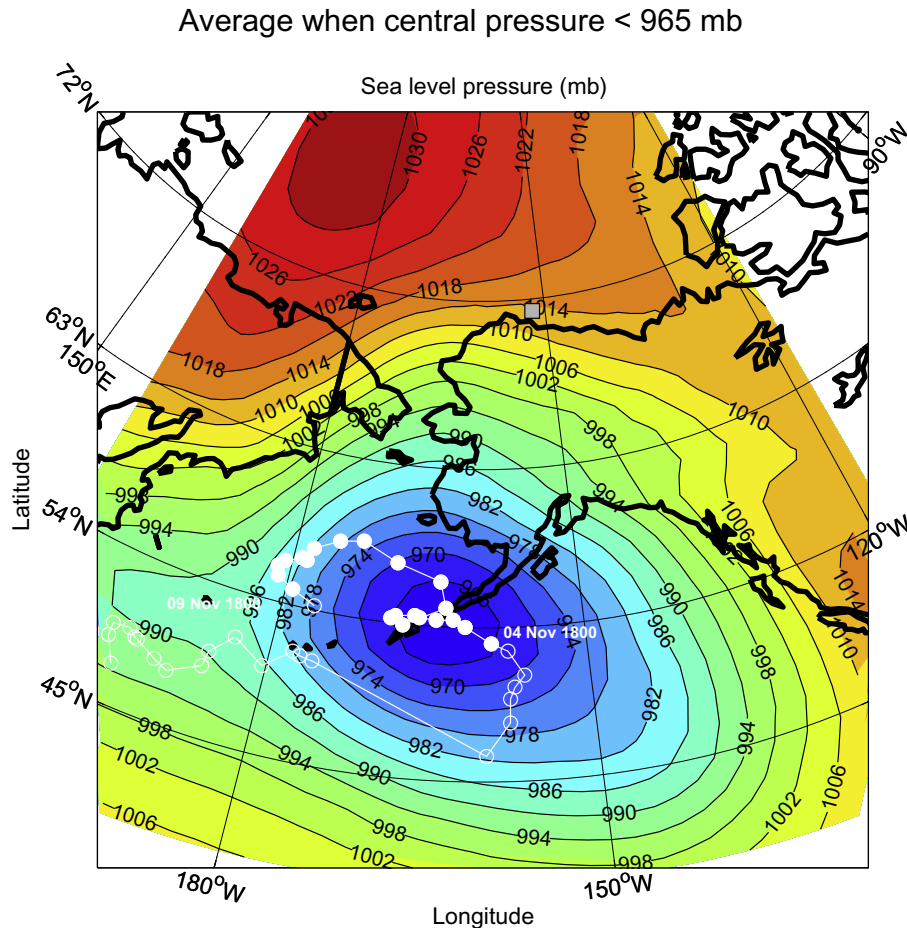


Fig. 3. Large-scale view of the Aleutian low pressure system that caused the upwelling event in the southern Arctic. The color and contours show the average NCEP SLP field during the time period when the central pressure of the storm was lower than 965 mb. The white line shows path of the storm. The circles denote the location of its center every 6 h. The 152°W mooring array is indicated by the gray square. Upwelling occurred at the array site during times when the white circles are filled. (For interpretation of the references to color in this figure legend, the reader is referred to the web version of this article.)

winds was indicative of the full suite of upwelling storms (11 major events) that occurred during the fall of 2002.

It is evident in each of the panels in Fig. 5 that the sharp transition to higher wind speeds in the Chukchi/Beaufort Seas corresponds to the ice edge. This is likely the result of a combination of the presence of an atmospheric frontal zone in the region, the reduced surface drag over the open water, as well as a reduction in static stability over the open water that leads to an increase in vertical momentum mixing. (It is difficult to rank these processes in order of their contribution to the higher wind speeds, which will require further analysis.) There is also an enhanced cross-ice edge air temperature gradient at this location (not shown), so part of the wind enhancement may be due to an ice breeze (Chu, 1987). However, the magnitude of this gradient is approximately 6 °C per 100 km, which would lead to a thermally driven ice breeze of only 2.5 ms⁻¹ (Chu, 1987). This is clearly not significant compared to the synoptically driven wind over the open water depicted in the four meteorological products.

The increased resolution of the WRF inner domain offers the opportunity to investigate the importance of smaller scale wind features—in particular, the effects of the Brooks Mountain Range (which is delineated by the white line in Fig. 5). Inspection of the both the sea-level pressure and surface wind fields reveals such an orographic impact (Fig. 5d). Note the enhanced easterly winds along the southern flank of the range, as well as the increased easterlies on the Beaufort shelf north of where the range nears the

coast. This “flow splitting” near the northeast knob of the range could be related to the corner effect discussed by Dickey (1961), who argued that super-geostrophic flow around the range would result in anomalously strong winds. However, Dickey’s (1961) choice of a cylindrical obstacle, as well as his assumption of irrotational flow, are questionable.

Another possibility is that the enhanced easterly flow over the shelf may be partly the expression of a phenomenon known as a tip jet (Doyle and Shapiro, 1999). Such jets form when large-scale flow rounds the end of a barrier, forming a narrow band of high winds that separates from the topography. This occurs near the southern tip of Greenland when extra-tropical cyclones interact with the high topography near Cape Farewell (Moore and Renfrew, 2005; Pickart et al., 2008; Våge et al., 2009). Since broad-scale Aleutian low storms—which are frequent in fall and winter—likely cause ambient flow to impinge on the Brooks Range, one might expect such tip jets to be common and significantly impact upwelling in the southern Beaufort Sea. This needs to be investigated in the future using a high resolution meteorological product such as the ETA model or possibly NARR.

3.3. Assessment of winds at the array site

It is of interest to compare the magnitude of the winds from the different meteorological products to that measured at the Pt. Barrow weather station (none of the met products assimilate the

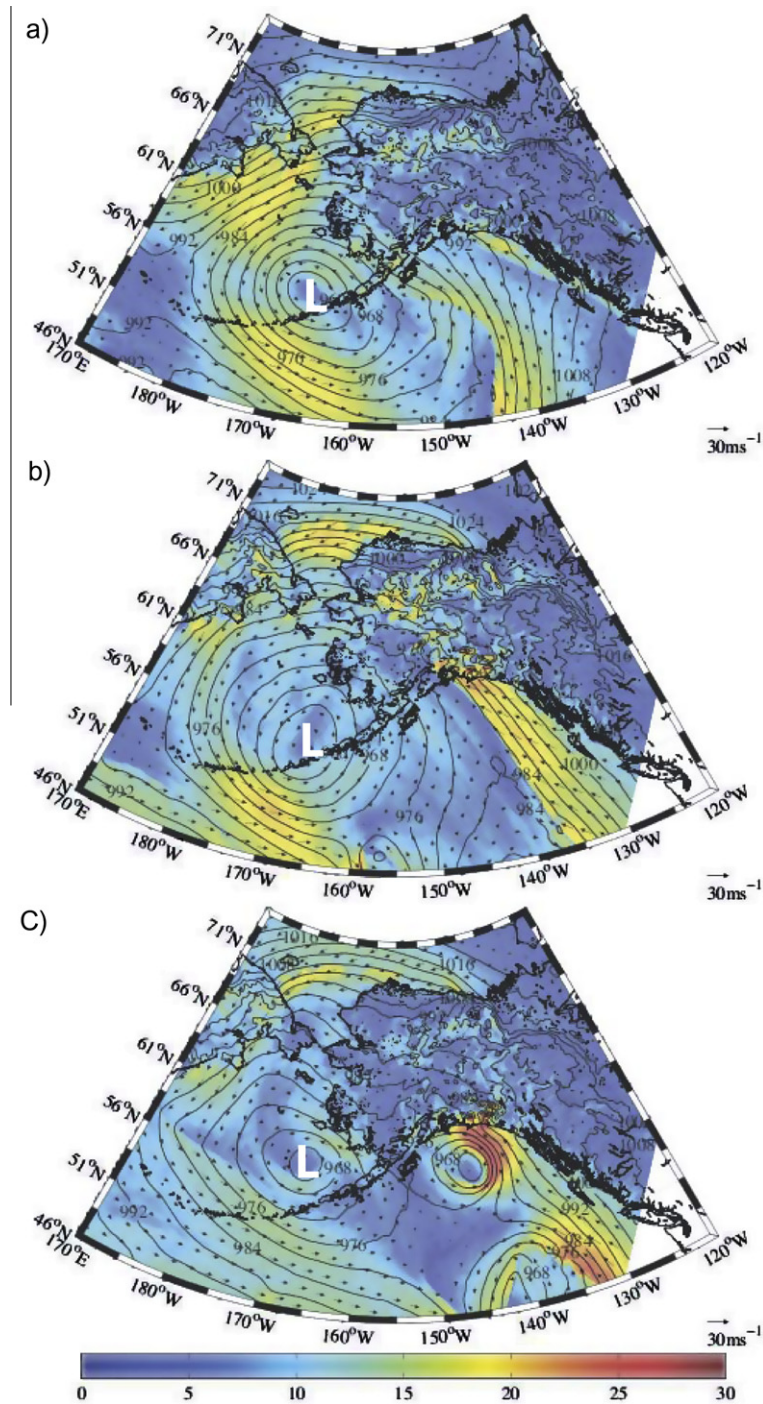


Fig. 4. Sea-level pressure (mb, contours), 10 m wind speed (ms^{-1} , color), and 10 m wind (ms^{-1} , vectors) from the WRF Domain 2 simulation at 0000Z on (a) November 5; (b) November 6; (c) November 7, 2002. The L marks the center of the parent low in each panel. (For interpretation of the references to color in this figure legend, the reader is referred to the web version of this article.)

Barrow winds). Such a comparison is shown in Fig. 6a. The timing of the storm is essentially the same for all of the timeseries, but the amplitude of the various products differs. In particular, the global NCEP and ETA signals are in line with the measured winds, while NARR underestimates and WRF overestimates the peak wind speeds. The discrepancy between NARR and NCEP is puzzling, since one would expect that the increased horizontal and temporal resolution afforded by NARR would result in more realistic winds. Inspection of Fig. 5 indicates that part of the issue is related to the location of the ice edge. In the NARR product the pack-ice

engulfs Pt. Barrow, in contrast to the other three products where the ice edge is east of Pt. Barrow (hence higher winds over the adjacent open water). This warrants further investigation of the integrity of NARR in the western Arctic.

According to all of the meteorological products, the winds associated with the storm were diminished at the mooring array site relative to Pt. Barrow (Fig. 6b). (The timing of the storm was the same, see also Nikolopoulos et al., 2009.) In light of the wind speed front associated with the ice edge, and the fact that the ice edge is west of the array site in all of the models, this decrease is not

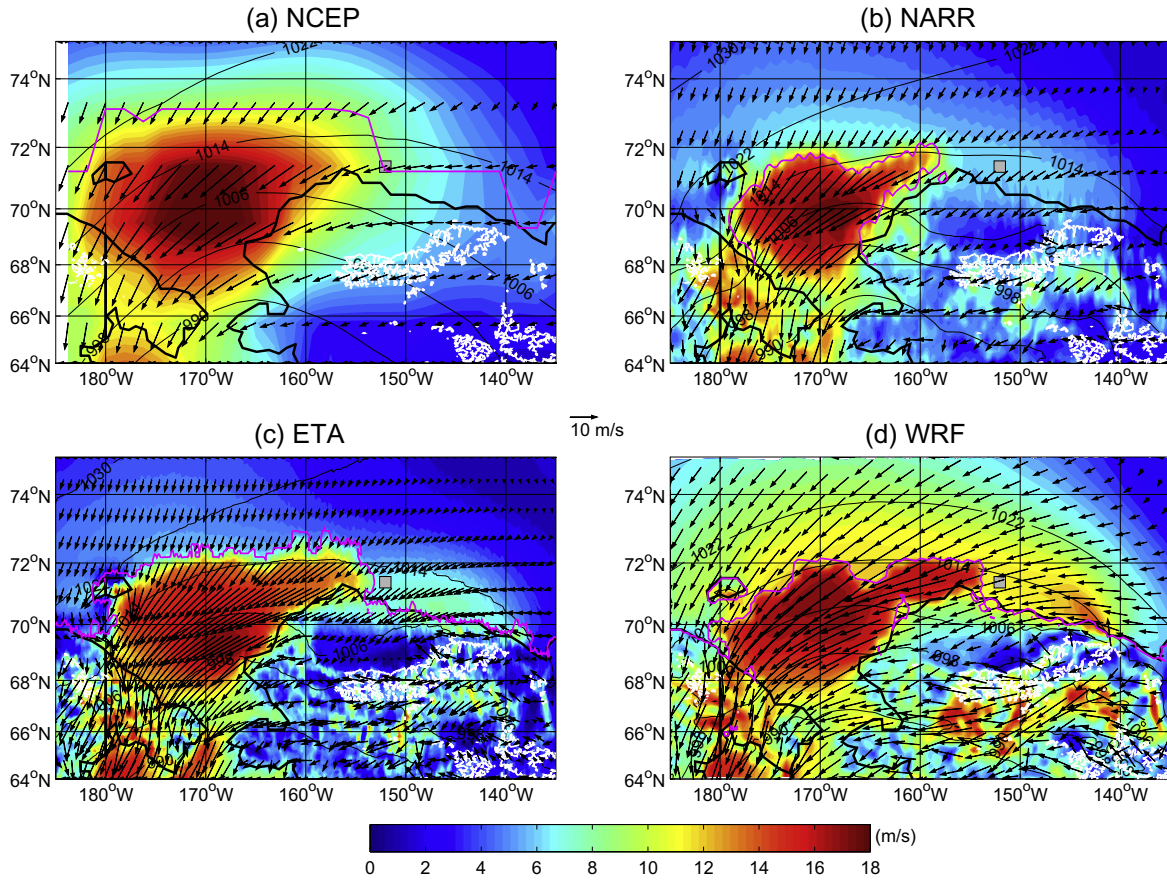


Fig. 5. Composite average of the 10 m wind field during the storm for the four meteorological products. Color denotes the wind speed, and the flow vectors are shown in black. The coast line is the thick black line, and the white line is the 1000 m height contour. The ice edge is denoted by the magenta line (the pack-ice is located north of the line). (a) NCEP; the time period of the composite is 4 Nov 1800Z–7 Nov 1200Z. (b) NARR; 4 Nov 1500Z–7 Nov 1500Z (c) ETA; 4 Nov 1800Z–7 Nov 1200Z. (d) WRF. 4 Nov 1500Z–7 Nov 0600Z. Note that the time interval of the four composites differs slightly due to the output constraints of the different models.

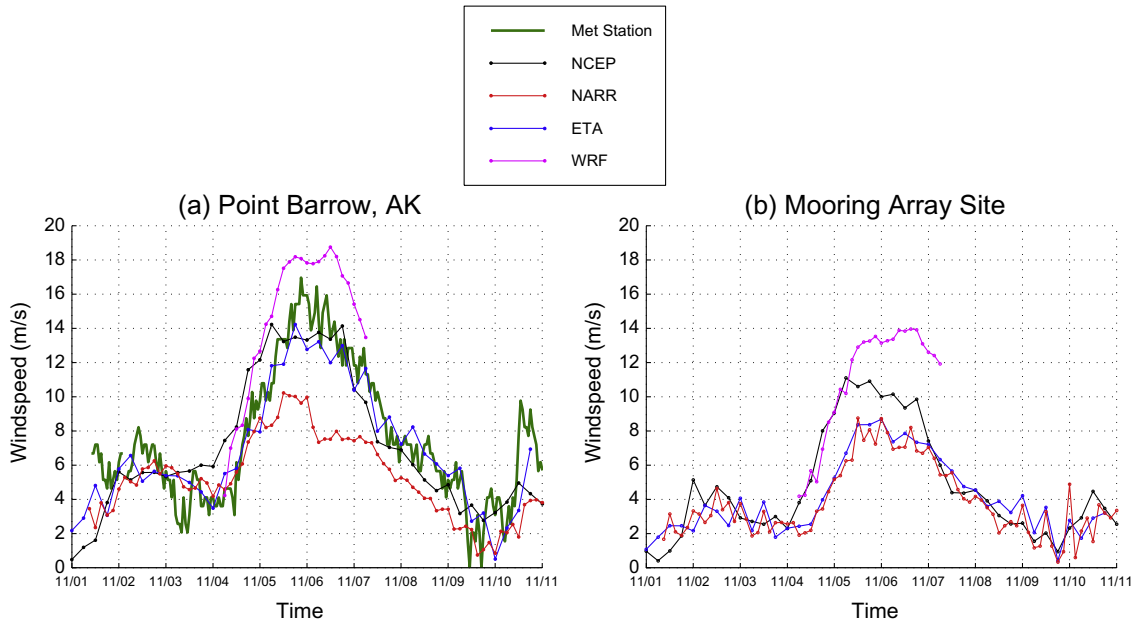


Fig. 6. Comparison of wind speed from the four meteorological products at (a) Pt. Barrow, AK, where the weather station winds are denoted by the green curve; and (b) the 152°W mooring array site.

surprising. In actuality, the ice concentration during the storm in the vicinity of the mooring array was about 50%, based on data from the Advanced Microwave Scanning Radiometer-Earth Observing System (AMSR-E) (see Pickart et al., 2009b). This implies that the models are likely underestimating the local winds for this storm. Furthermore, the tip jet discussed above is essentially absent in NCEP and NARR, and likely underestimated in ETA. Inclusion of this effect in these three models would enhance the local winds and lessen their discrepancy relative to the local WRF winds. The overall message then seems to be as follows: (1) the winds at the array site for the storm in question were probably closer to those measured at Pt. Barrow than suggested by Fig. 6b; (2) the tip jet caused by the Brooks Range may be an important effect at the array site; (3) the location of the ice edge should be considered when using the Pt. Barrow wind record as a proxy for the winds at the array site. For what follows, we will use the Barrow wind record to represent the wind-forcing of the storm.

4. Response at the Beaufort shelfbreak

In the absence of forcing, the Beaufort shelfbreak current flows to the east year-round (Fig. 7; Nikolopoulos et al., 2009). During a 1–2 month period in late-summer/early-fall it is surface-intensified and advects warm, fresh Alaskan Coastal Water (Mountain, 1974; von Appen and Pickart, 2010); at this time it can be considered the extension of the Alaskan Coastal Current beyond Point Barrow. Over the remainder of the year it is bottom-trapped, carrying denser, colder Pacific-origin waters (including Chukchi Summer Water and Winter-transformed Water). The core of the current is situated at the shelfbreak (Fig. 7), but during the late-autumn and winter months the current often develops a deep “tail” that extends to depths >500 m. As discussed in Nikolopoulos et al. (2009), these deep extensions of the jet occur after upwelling storms and accelerate the Atlantic Water on the continental slope. They are prevalent enough that their signature appears in the year-long mean section (Fig. 7). One of the main goals of the present paper is to provide an explanation of these deep flow extensions.

A typical sequence of events occurs in the Beaufort shelfbreak jet system when the wind blows from the east at speeds exceeding roughly 6–7 ms^{-1} (Pickart et al., 2009b). The flow reverses to the west, followed by upwelling of warm and salty water. The presence

of pack-ice does not seem to prohibit the occurrence of these events, although the magnitude of the ocean response is dampened when the ice concentration is near 100% (Pickart et al., 2009b). Note that this casts doubt on the appropriateness of the Chapman and Carmack (2003) characterization of the pack-ice as impenetrable to the wind in this region, at least in recent years. On the other hand, land-fast ice will undoubtedly shelter the water column completely from the wind. Although the land-fast ice edge typically resides on the inner Beaufort shelf near the 20 m isobath, there are times when it extends significantly seaward, even beyond the shelfbreak (Mahoney et al., 2007).

4.1. Observations of the November 2002 storm event

We now use the Beaufort slope mooring array data to describe the response of the shelfbreak jet to the upwelling storm of early November, 2002. In light of the statistical results of Pickart et al. (2009b), the response was typical in its overall features, but there were unique aspects since this particular storm was one of the strongest during the year. As mentioned above, the ice concentration at the time of the event was roughly 50%. The timing of the velocity and hydrographic response of the water column is shown in Fig. 8. Prior to the storm the peak velocity of the eastward-flowing shelfbreak jet was order 60 cm s^{-1} . Interestingly, the jet started to spin-down prior to the onset of the strong winds (by more than 24 h). This may have led to the surprisingly fast flow reversal of the jet, which occurred nearly in phase with the wind record (Fig. 8a). (Statistically, over the year-long record, the reversed flow due to storms lagged the local winds by 8 h, see Pickart et al., 2009b). Although the jet rebounded fairly quickly as the winds subsided (Fig. 8a), the core depth of the re-established eastward flow deepened significantly (investigated in detail below).

The occurrence of upwelling is displayed here as a timeseries of the minimum depth of the 0°C contour within the vertical plane (Fig. 8). As one can see, the timing of the upwelling followed the local wind field closely, with a lag of 18 h (this was true statistically as well over the year-long record). The magnitude of upwelling was such that the 0°C contour rose by 160 m. By way of comparison, Carmack and Kulikov (1998) observed that Atlantic Water was advected 130 m upslope during an upwelling event on the Canadian Beaufort shelfbreak. Note in Fig. 8 that the

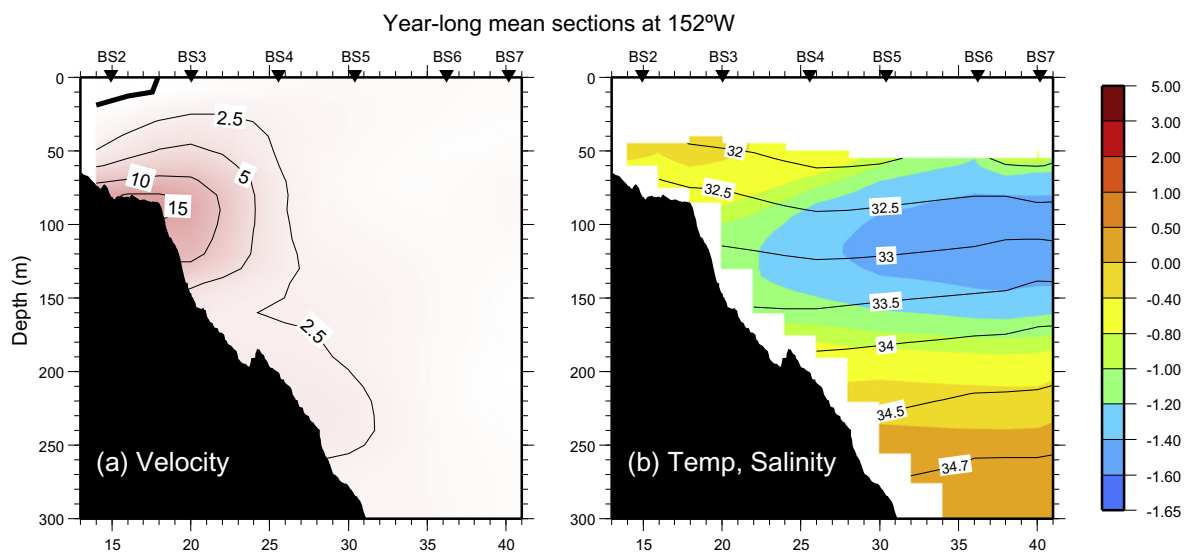


Fig. 7. Year-long mean vertical sections from the 152°W mooring array. (a) Alongstream velocity (cm s^{-1} , where positive is along 125°T). (b) Potential temperature (color, $^\circ\text{C}$) with salinity (contours) overlaid. The means were computed over the time period 2 August 2002–31 July 2003 (from Nikolopoulos et al. (2009)). (For interpretation of the references to color in this figure legend, the reader is referred to the web version of this article.)

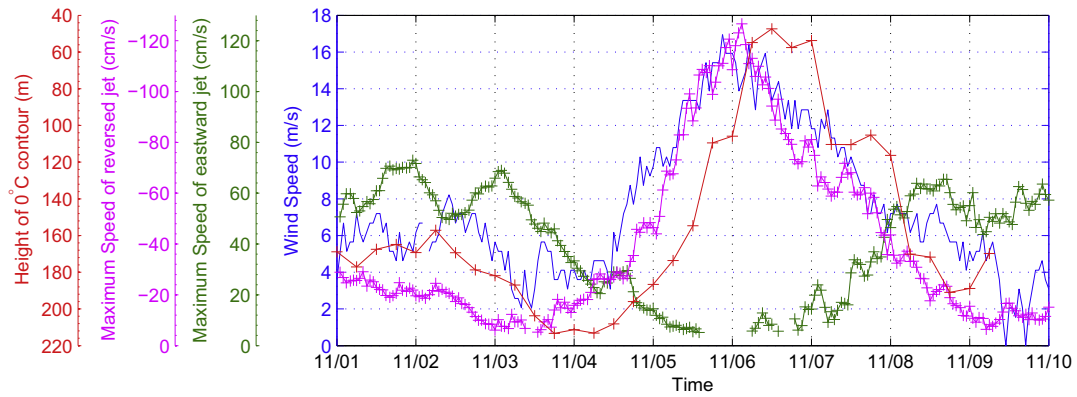


Fig. 8. Timeseries of the boundary current at 152°W during the storm. The blue curve is the wind speed at the Pt. Barrow meteorological station; the green curve is the maximum speed of the eastward jet; the magenta curve is the maximum speed of the reversed jet (at whatever depth it occurs); the red curve is the minimum height of the 0 °C isotherm. (For interpretation of the references to color in this figure legend, the reader is referred to the web version of this article.)

relaxation of the 0 °C contour was not quite complete at the end of the storm (another upwelling event occurred soon after the conclusion of the event analyzed here). The close correspondence between the windspeed timeseries at Pt. Barrow and the velocity and hydrography of the shelfbreak jet in Fig. 8 suggests that a large part of the response of the jet is due to the local wind field (as opposed to an entirely remote response to winds elsewhere along the slope).

An effective way to describe the evolution of the boundary current over the course of the storm is through the use of composite vertical sections. We divided the upwelling event into five stages

plus an “initial condition”, which are presented in Figs. 9–14. Before discussing the sequence of composites, it is important to explain the observational coordinate system that was used in constructing them. Our aim is to consider the flow in the along-stream and cross-stream directions, rather than alongslope and cross-slope (which are dictated by the orientation of the topography). While there are various ways that one might define the alongstream direction, we chose the following approach (the results are not qualitatively sensitive to this choice). Three different rotation angles were employed: one corresponding to the boundary current before the onset of the storm, a second associated with

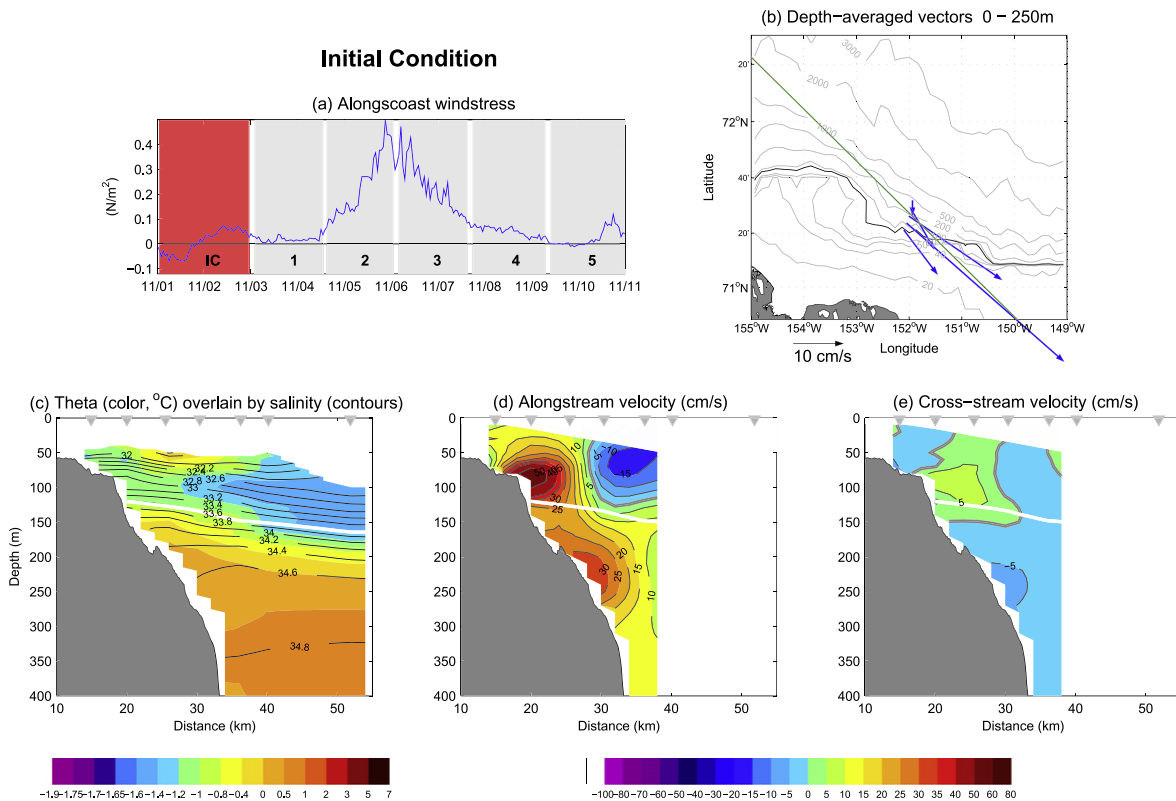


Fig. 9. Composite average fields before the start of the storm. (a) Alongcoast windstress at the Pt. Barrow meteorological station (positive stress corresponds to easterly wind). The “initial condition” and five stages of the storm are marked in gray. The red denotes the time period of the composite. (b) Depth-averaged flow vectors at the mooring sites. The straight green line is the alongstream direction (see text). The 85 m isobath, which roughly corresponds to the shelfbreak, is highlighted in black. (c) Average potential temperature (color) overlain by average salinity (contours). The thick white line denotes the boundary between the shallower Pacific Water and deeper Atlantic water (33.64 salinity contour, see Nikolopoulos et al., 2009). (d) Alongstream velocity, where positive is eastward. (e) Cross-stream velocity, where positive is northward. (For interpretation of the references to color in this figure legend, the reader is referred to the web version of this article.)

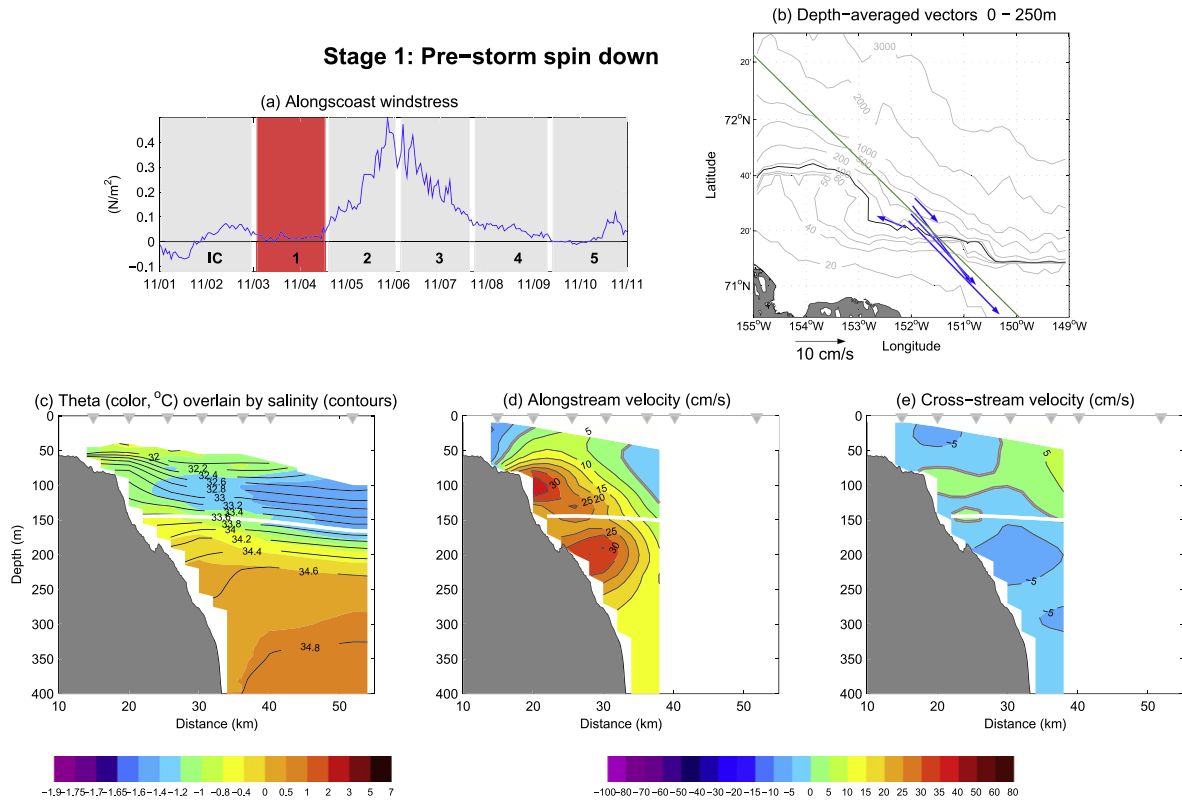


Fig. 10. Composite average fields during the first of the five stages of the storm. The presentation is the same as in Fig 9.

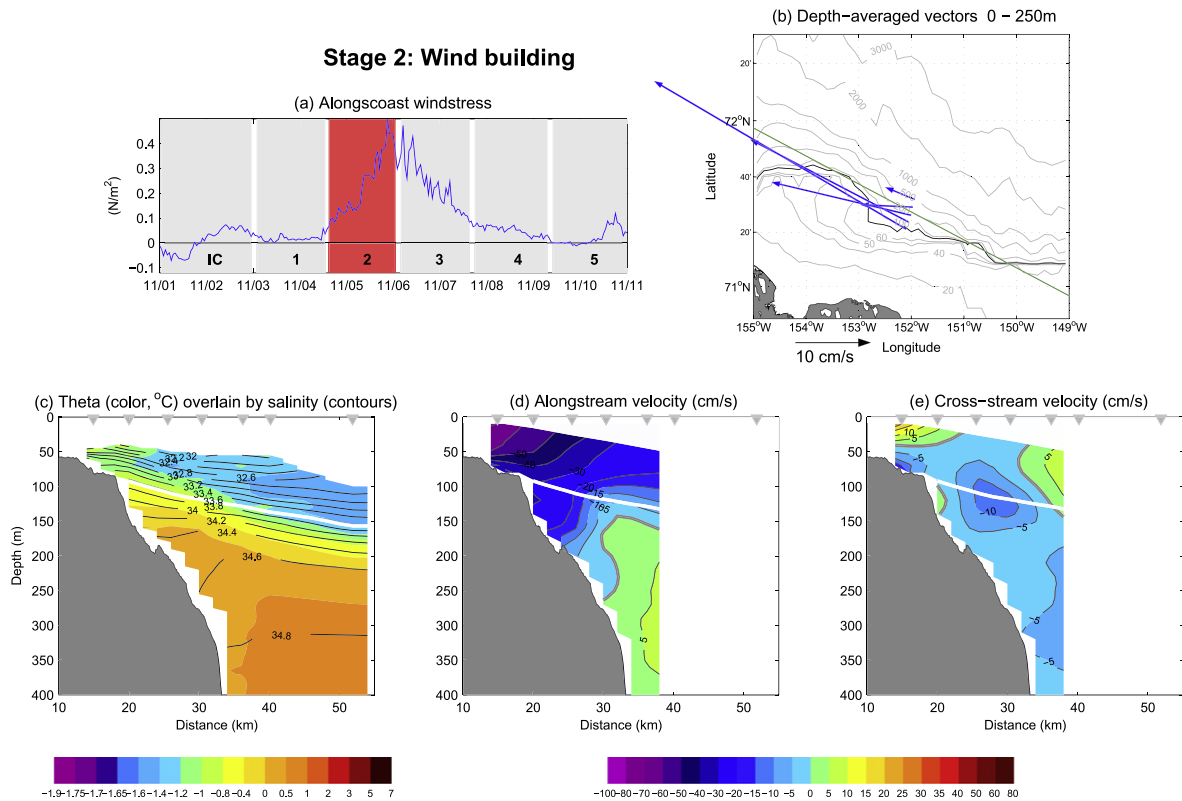


Fig. 11. Composite average fields during the second of the five stages of the storm. The presentation is the same as in Fig 9.

the period of high winds, and a third appropriate to the current after the conclusion of the storm. To determine the first angle, a

single mean flow vector was computed for the period of the initial condition (Fig. 9a). In particular, the flow was averaged over the

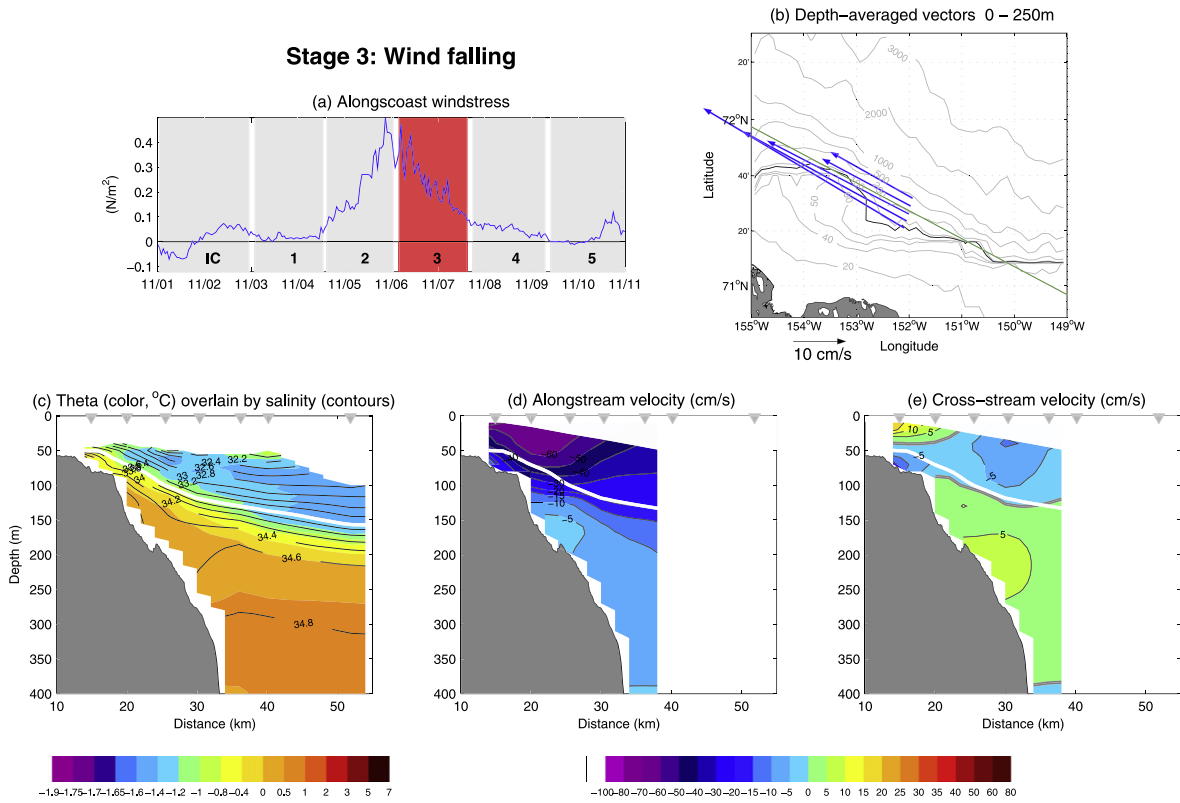


Fig. 12. Composite average fields during the third of the five stages of the storm. The presentation is the same as in Fig 9.

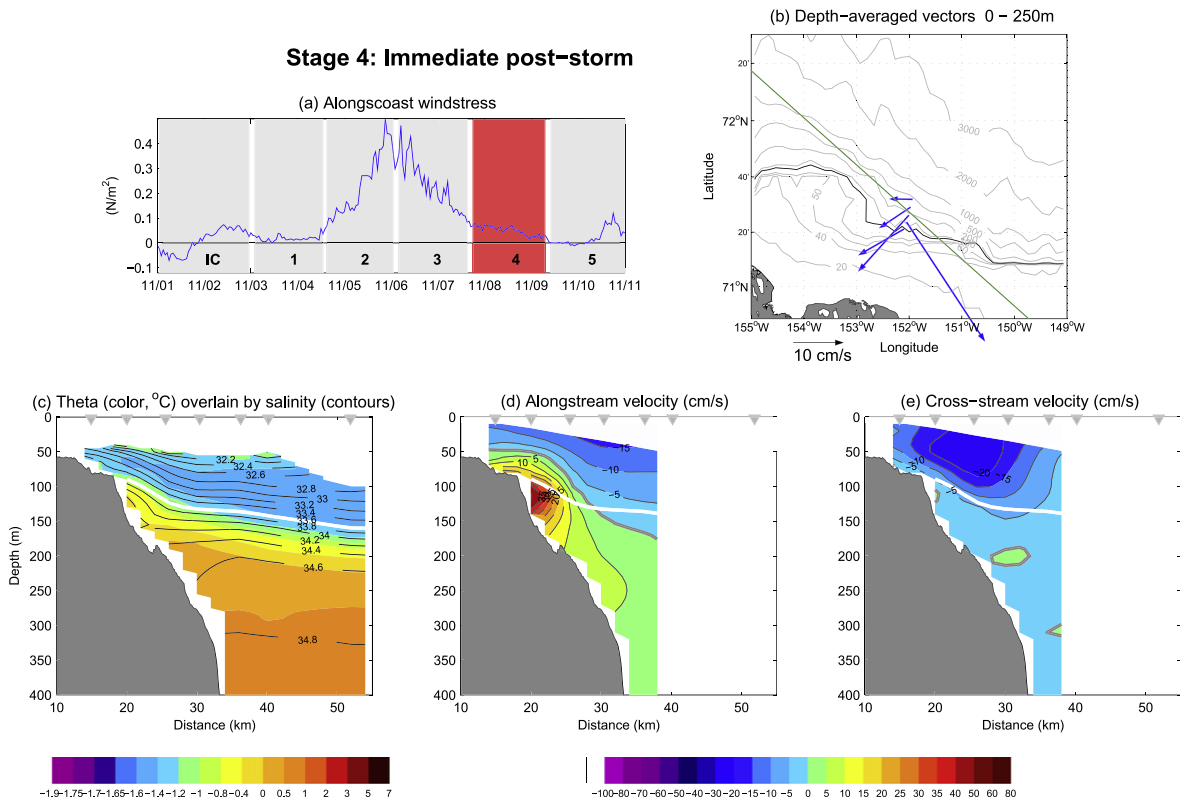


Fig. 13. Composite average fields during the fourth of the five stages of the storm. The presentation is the same as in Fig 9.

depth range 0–250 m at each site, then the lateral average of these five vectors was computed. The orientation of the resulting mean

vector was taken as the alongstream direction for both the initial condition as well as stage 1. The analogous calculation was done

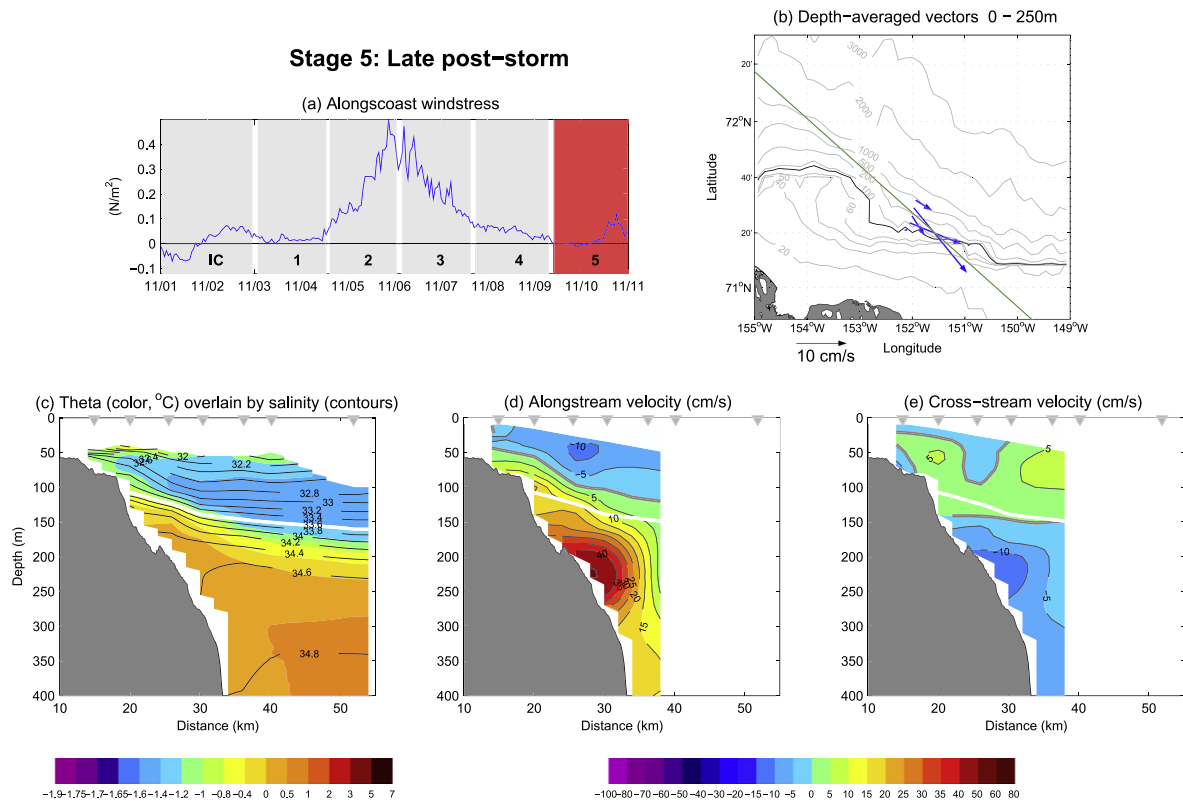


Fig. 14. Composite average fields during the final stage of the storm. The presentation is the same as in Fig. 9.

for the period of strong winds (stages 2 and 3), then for the final stage (which was applied to stages 4 and 5). The reason for using a different initial and final angle instead of a single alongstream direction for the entire period is that, in the latter case, the cross-stream flow is similar in structure to the alongstream flow both before and after the storm, which is an indication that the stream coordinate direction was not appropriately chosen for those time periods (i.e. some of the alongstream flow was being projected onto the cross-stream direction).

The initial condition of the boundary current is shown in Fig. 9. In the figure (and for the subsequent composites as well) we show the alongcoast windstress from the Pt. Barrow meteorological station, where the time period of the composite has been highlighted in red² (Fig. 9a). Alongside this are the mean velocity vectors at the mooring sites averaged over the top 250 m of the water column (Fig. 9b). The orientation of the alongstream direction for the composite is shown by the green line. The mean vertical section of potential temperature (color) overlaid by salinity (contours) is displayed in Fig. 9c, and the sections of alongstream and cross-stream velocity are shown in Fig. 9d and e, respectively. In the sections the viewer is looking to the west, and positive velocities are eastward (alongstream) and northward (cross-stream).³ Before the onset of the storm the shelfbreak jet was flowing strongly to the east ($>50 \text{ cm s}^{-1}$), with a second deeper core near 250 m depth. The presence of the deep core is the result of an earlier upwelling event (see below). For the most part the mean flow is uni-directional with a weak cross-stream component (note that by definition the integrated cross-stream flow over the section should be near-zero). The temperature section reveals a slight uplift of the

Atlantic Water against the continental slope (also the result of the previous upwelling event). The nominal boundary between the Pacific Water and the Atlantic Water is denoted by the thick white line in Fig. 9c. This corresponds to a potential temperature of $-1.26 \text{ }^\circ\text{C}$ and salinity of 33.64, as determined by Nikolopoulos et al. (2009) using the year-long mooring hydrographic data. In particular, Nikolopoulos et al. (2009) used the potential vorticity maximum at the base of the Pacific winter water as the water mass boundary, which corresponds closely to that determined using the nitrate-phosphate relationship (see Jones et al., 2003). As seen in Fig. 9d, the shallow velocity core near the shelfbreak is comprised entirely of Pacific Water, whereas the deep extension is Atlantic Water.

During stage 1 (Fig. 10) the shelfbreak jet began to change despite the fact that the alongcoast windstress remained weak. That is, the jet started to spin-down prior to the arrival of the high winds (mentioned above, see Fig. 8). Not only did the eastward-flowing core of the jet decrease by 30%, but the flow at the inner-most mooring (i.e. the outer-shelf) reversed to the west. Cross-stream velocities remained weak, and the Atlantic Water slumped to greater depths (the boundary between the Atlantic and Pacific Water, indicated by the white line, became more level across the section). It is worth noting that the winds at Pt. Barrow shifted to an easterly orientation roughly 24 h prior to this composite, which suggests that even weak easterly winds can impact the shelfbreak jet. Another potential contributing factor in the initial spin-down is that the post-storm adjustment from the previous upwelling event was starting to wane (see Section 4.2).

The next two stages of the storm correspond to the period of high winds. Fig. 11 corresponds to the period of building winds, and Fig. 12 covers the period of falling winds. As the winds increased (stage 2) the flow of the shelfbreak jet reversed at all sites, with the strongest response at the inner-most location (instantaneously the flow exceeded 120 cm s^{-1}). The composite

² For interpretation of color in Figs. 3–21, the reader is referred to the web version of this article.

³ For ease of reference we refer to these directions throughout the paper as east and north, rather than east-southeast and north-northeast.

hydrographic section indicates that the upwelling process had begun, although the deepest isohalines were still oriented downwards towards the slope. The secondary circulation associated with the storm became well-developed, with offshore Ekman flow in the upper-layer and onshore return flow at depth. The strongest cross-stream flow occurred at the outer-shelf (note that the blanking region of the ADCPs partly masked the signature of the near-surface flow seaward of the shelfbreak). As seen in Fig. 11e, the Ekman circulation cell occupies the entire water column at the inshore-most mooring; i.e., the secondary flow is not confined to thin surface and bottom boundary layers. Farther offshore there is no evidence of a bottom boundary layer at all, and the onshore flow occupies a significant portion of the interior water column.

As the wind reaches its peak and begins to decrease (stage 3), the integrated flow of the shelfbreak jet is nearly uni-directional to the west (Fig. 12b). Unlike the previous stage, the strongest alongstream flow now occurs at the shelfbreak (not on the shelf). At this point in time the upwelling has reached its maximum extent and Atlantic Water is found on the shelf. However, there is an aspect of the upwelling that indicates that this process is not strictly two-dimensional. Note on the upper slope the small pool of salty water delimited by the 34.6 isohaline. Instantaneously this pool is much more pronounced, denser by $.3 \text{ kg m}^{-3}$ than the water immediately downslope (not shown). This is a ubiquitous feature of upwelling at the array site (over many events), as is the sharp downward bend of the deep isopycnals farther down the slope (note the 34.6 isohaline, Fig. 12c). Further evidence of the non-two-dimensional nature of the water column response is seen in the cross-stream velocity composite (Fig. 12e). As in the previous stage, the Ekman cell is strong on the outer-shelf, but offshore of this the deep cross-stream flow is directed offshore. In fact, the zero isochore of cross-stream velocity corresponds closely to the Atlantic–Pacific water mass boundary. In other words, none of the deep Atlantic Water is progressing upslope at the array site. This implies that the upwelled water present on the shelf came from a location well to the east of the mooring array, consistent with the theory of Allen (1976). This is discussed further in the modeling section below.

After the winds subside, the eastward-flowing shelfbreak jet begins to spin up again and the upwelling starts to diminish (stage 4, Fig. 13). However, there are some surprising aspects of this process. Firstly, note that the bulk of the eastward flow of the jet is Atlantic Water, not Pacific Water (unlike the initial condition, Fig. 9d). In the region of this eastward flow the isopycnals remain sloped upwards towards the coast. Secondly, there is onshore flow throughout the water column (note the depth integrated vectors of Fig. 13b). In fact, the magnitude of the secondary circulation is larger than the primary circulation at all of the sites except near the shelfbreak. Again it is clear that the circulation is not two-dimensional in character. The nature and cause of the onshore flow and its relation to the spin up of the eastward current is discussed below in the framework of the model.

In the final stage of the upwelling event (stage 5, Fig. 14), the shelfbreak jet deepens, with the strongest flow now centered near 225 m (well into the Atlantic layer). As time progresses this deep extension weakens (this was happening in the initial condition composite of Fig. 9d, subsequent to the previous storm). We refer to this eastward flow as the “relaxation flow”. Note in Fig. 14d that the Pacific Water is starting to accelerate, which continues beyond the time period of this composite until the shelfbreak jet of Pacific Water is fully re-established (as in the initial condition). Note also in Fig. 14c that the Atlantic Water has not yet returned to its normal depth. Hence, both in terms of the hydrography and the primary circulation, the upwelling event is not yet complete at stage 5. The cross-stream flow, however, has decreased to pre-storm levels. Note that the onshore flow of the previous stage

seems to have fed both the westward upper-layer flow that persists after the storm, as well as the eastward relaxation flow at depth. No attempt has been made to assess the precise mass balance, although this is addressed below using the model.

It is worth noting that the relaxation jet may provide an explanation for the so-called Beaufort Undercurrent identified by Aagaard (1984). Using hydrographic sections and sparsely-spaced moorings along the Alaskan Beaufort slope, Aagaard (1984) argued that a deep-reaching, eastward-flowing boundary current existed seaward of the shelfbreak. He noted that the thermal wind shear (upward-sloping isopycnals towards the continental slope) was associated with salty water onshore, consistent with upwelling. As discussed above, the hydrographic signature of the upwelling event studied here persisted beyond the end of the storm (stages 4 and 5), providing the right sense of thermal wind shear. As presented by Nikolopoulos et al. (2009), the relaxation jet is a ubiquitous feature of upwelling events throughout the fall and winter, and the signature of the jet is found as deep as 700 m. This suggests that the Beaufort Undercurrent may be a seasonal phenomenon associated with upwelling storms, rather than a component of the large-scale circulation of the western Arctic. As seen in Fig. 7, the year-long mean eastward flow is strongest near the shelfbreak, although there is a distinct (albeit weak) signature of the relaxation jet.

To summarize, the salient aspects of the upwelling event revealed by the observations are as follows: (1) the Pacific Water shelfbreak jet is readily reversed by the easterly winds, with peak westward speeds in the water column exceeding 1 ms^{-1} ; (2) a strong Ekman circulation develops at the outer-shelf, but seaward of this the secondary flow is not two-dimensional; (3) Atlantic water is upwelled onto the shelf; (4) following the storm, a deep eastward relaxation flow of Atlantic Water spins up—presumably fed by onshore flow from the basin—prior to the re-establishment of the Pacific Water shelfbreak jet. We now elucidate this sequence of events using a simple numerical model.

4.2. Modeling a storm event

The numerical model used in this study is the MIT general circulation model (Marshall et al., 1997). It solves the hydrostatic, primitive equations of motion on a uniform Cartesian, staggered C-grid with level vertical coordinates. A partial cell treatment of the bottom topography is accurate for steep topography in the presence of stratification (Adcroft et al., 1997), expected to be important for the wind-driven upwelling problem. To address the occurrence of upwelling on the Beaufort slope the model was configured as a rectangular domain with a shelf and slope along the southern boundary. Although quite idealized compared to the Alaskan Beaufort Sea, this configuration reproduces many of the essential features of the observations described above, and allows for a clear demonstration of the controlling physics. This configuration also demonstrates that such a general response to wind events can be expected in many coastal upwelling areas and is not, in the broadest sense, particular to the region of the mooring data.

After studying the idealized model, we consider a second configuration of the MIT model that includes realistic bottom topography of the Chukchi and Beaufort seas, forced by NCEP winds (Section 5.1). Importantly, the semi-realistic model demonstrates similar behavior at the mooring location to both the observations and the idealized model configuration. While the simplified geometry of the idealized calculation allows us to isolate more effectively the governing physics, the larger, more realistic domain enables us to assess the impact of such storm events on the broad scale circulation of the Chukchi and Beaufort Seas.

4.2.1. Idealized domain

The simplified configuration considered first is a rectangular domain extending 3400 km in the zonal direction and 2725 km in the meridional direction, with closed boundaries on all sides. The shelf is approximately 25 km wide, sloping linearly from 50 m at the southern boundary to 100 m at the shelfbreak. The shelf transitions to the interior basin depth of 450 m with a hyperbolic tangent function over a lateral scale of 12 km (the topography is shown in Fig. 15). The horizontal resolution is 5 km in the zonal direction and varies in the meridional direction from 2 km (within 250 km of the southern boundary) to 5 km in the mid-basin and 10 km in the northern-most portion of the domain. Although we are interested in the response only near the southern boundary, we have extended the domain far enough offshore that the wind-driven response along the northern boundary does not influence the behavior near our area of interest. There are 30 levels in the vertical spaced 10 m apart between 0 and 40 m, 5 m apart between 40 m and 130 m, and gradually increasing to 50 m spacing between 200 and 450 m depth. The calculations are carried out on a beta-plane with $f = f_0 + \beta y$, where $f_0 = 1.4 \times 10^{-4} \text{ s}^{-1}$, $\beta = 2 \times 10^{-11} \text{ m}^{-1} \text{ s}^{-1}$, and y is the distance northward from the southern boundary of the model. Density is determined by salinity only, which is appropriate for this location in the Arctic during fall. The initial stratification is piecewise uniform in the vertical, $N^2 = 2 \times 10^{-4} \text{ s}^{-2}$ in the upper 175 m and $N^2 = 0.5 \times 10^{-4} \text{ s}^{-2}$ deeper than this. The initial salinity profile is shown in Fig. 15 (upper 300 m only).

The model incorporates second order vertical viscosity of $10^{-4} \text{ m}^2 \text{ s}^{-1}$ and second order vertical diffusivity of $10^{-5} \text{ m}^2 \text{ s}^{-1}$. The vertical diffusion is increased to $1000 \text{ m}^2 \text{ s}^{-1}$ for statically unstable conditions in order to represent vertical convection. Horizontal viscosity is parameterized as a second order operator, A_h , determined by a Smagorinsky (1963) closure as

$$A_h = (\nu_s/\pi)^2 L^2 D. \quad (1)$$

The parameter ν_s is a non-dimensional coefficient taken here to be 2, L is the grid spacing, and D is the deformation rate, defined as

$$D = [(u_x - v_y)^2 + (u_y + v_x)^2]^{1/2}, \quad (2)$$

where u and v are the resolved horizontal velocities and subscripts denote partial differentiation. A linear bottom drag of $C_d = 10^{-4}$ is included, and the lateral boundary conditions are no-slip for velocity and no-flux for temperature and salinity. The results have been found to be relatively insensitive to the specific choice of subgrid-

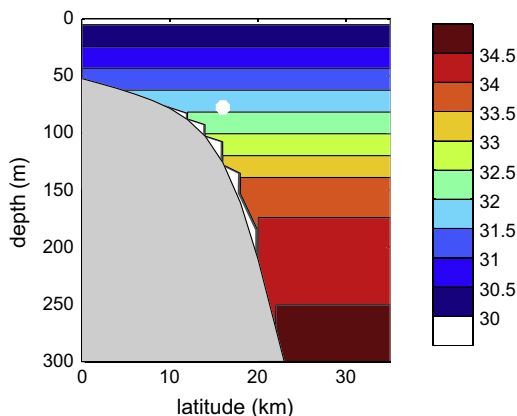


Fig. 15. Initial salinity profile and bottom topography along the southern boundary, for the idealized model. The white triangles are an artifact of the contouring and the discreet representation of the bottom topography by the model grid. The white dot marks the latitude/depth location of the longitude–time plots shown in Fig. 18.

scale mixing parameterizations. Our aim here is to demonstrate that a fairly simple model configuration is able to reproduce the basic elements observed at the mooring location.

To mimic the November 2002 storm, the idealized model is forced with a zonal wind stress of maximum strength -0.4 N m^{-2} along a portion of the southern boundary (i.e. towards the west). The wind is uniform in the zonal direction between 1000–2000 km longitude and 0–2000 km latitude, and zero outside this region. The model is run for 20 days. The domain is sufficiently large that a signal originating from the offshore boundary where the wind-forcing is active would take 23 days (at a wave speed of 2.5 m/s) to reach the region of interest along the southern boundary, so the effects of the closed offshore boundaries on the calculation are minimal. The wind is applied for the first 4 days and is then ramped down to zero over a time scale of 0.5 days in order to investigate the relaxation response. In this idealized simulation there is no pre-existing eastward shelfbreak jet. The current was omitted in order help isolate the lowest order dynamics at work—in particular, those associated with the post-storm relaxation flow. The more complex model presented in Section 5.1 includes the inflow from Bering Strait and hence the shelfbreak current.

4.2.2. Response during the storm

Vertical cross-sections constructed from the model at 1500 km longitude during the storm are shown in Fig. 16 (on day 4 before the wind is ramped down). Similar to the observations, the easterly winds force a swift, surface-intensified westward jet, which is strongest on the mid-shelf. An offshore Ekman transport in the upper layer induces upwelling along the coast which brings salty water from the mid-slope onto the shelf. In contrast to the observations, the surface and bottom boundary layers in the secondary circulation are vertically distinct. Because the water advected offshore in the surface Ekman layer was upwelled at the coast, and is denser than the ambient upper-layer water, vertical convection forms a mixed layer that extends to about 40 m depth. Such a uniform layer is not resolvable by the profiling CTD moorings because the depth of the top floats was approximately 45 m.

The surface Ekman circulation continues to advect dense water offshore which results in increasingly salty water being brought onto the shelf, while the sea surface elevation drops near the coast. Hence, there is an onshore pressure gradient at the surface, and an offshore density gradient at depth. This is why the westward jet is surface-intensified. An important aspect of the flow is that the secondary circulation is not two-dimensional: Some of the offshore transport carried in the Ekman layer is supplied by the convergence of the alongstream velocity, not the cross-stream velocity. This is a well known consequence of the three-dimensional nature of the flow and the propagation of information from the westward limit of wind-forcing towards the east (e.g. Allen, 1976). It is also consistent with the observation noted above that the cross-stream velocity deeper than the shelfbreak was directed offshore near the height of the storm (Fig. 12), implying a non-two-dimensional mass balance.

4.2.3. Adjustment after the storm

The model vertical sections (at the same location as above) after the storm are shown in Fig. 17 (for day 7, which is three days after the wind-forcing started ramping down). While the pycnocline has relaxed below a depth of approximately 100 m (Fig. 17a), the isohalines on the shelf have changed little since day 4. The biggest change is in the circulation. The zonal velocity is now eastward along the bottom with the maximum located near the shelfbreak (Fig. 17b), while the zonal flow near the surface is still westward. The vertical shear in alongstream velocity is approximately 40 cm s^{-1} over 100 m depth, very similar to what it was outside

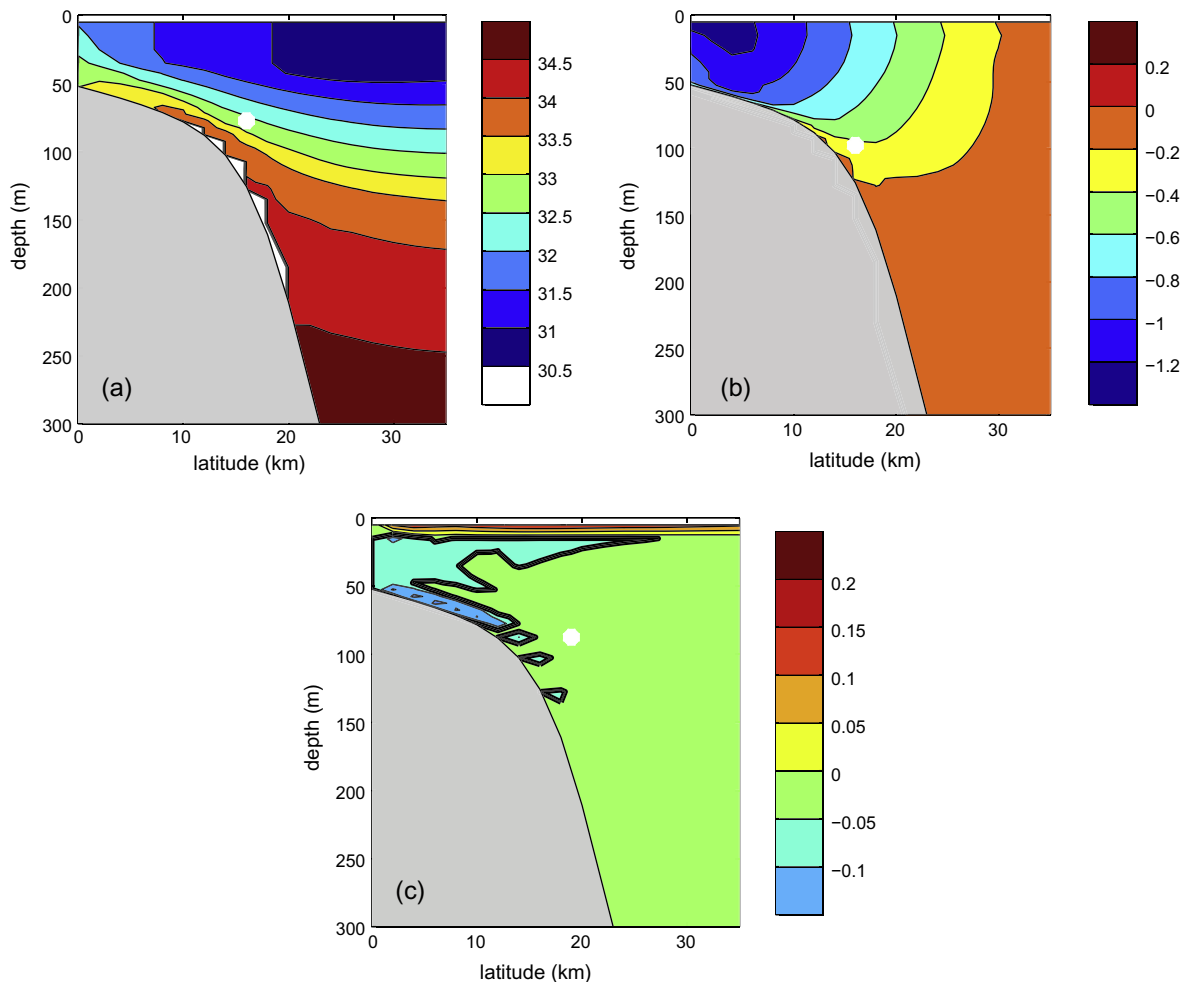


Fig. 16. Sections at 1500 km longitude on day 4 of (a) salinity (contour interval 0.5), (b) zonal velocity (contour interval 0.1 m s^{-1}), (c) meridional velocity (contour interval 0.05 m s^{-1}).

the bottom boundary layer at the end of wind-forcing on day 4. This is consistent with the salinity field, which showed little change in the baroclinic pressure gradient above 100 m since day 4. The cross-stream velocity (Fig. 17c) is now weakly southward in the upper layer over the shelfbreak ($O(1 \text{ cm s}^{-1})$) and northward in the bottom boundary layer (consistent with an Ekman layer below an eastward flow).

One of the primary reasons for undertaking the modeling study was to shed light on the nature and cause of the post-storm (eastward) relaxation flow observed by the moorings. The idealized model clearly captures this phenomenon (Fig. 17b). An effective tool for investigating the evolution of the model fields is the use of longitude–time plots. These are shown for salinity, along- and cross-stream velocity, and sea surface height in Fig. 18 for the region near the shelfbreak (the locations of the time series are given in Figs. 16 and 17). The salinity (Fig. 18a) initially increases linearly in time due to upwelling of deep waters. This rapid increase then switches to a nearly steady state as the influence of the finite extent of wind-forcing propagates eastward. The approximate propagation speed is indicated in the figure by the two solid black lines (elaborated on below): the lower line emanates from the edge of the storm when the wind is turned on, and the upper line does so when the wind is turned off. By the time the wind ceases after four days (denoted by the thin white line), the transition away from two-dimensional flow has propagated most of the way across the wind-forcing region. The zonal velocity (Fig. 18b) shows a

similar transition from the time-dependent two-dimensional solution, in which the velocity grows in time (independent of longitude) to a more steady regime where the zonal velocity evolves slowly after the transition has passed. Note that after the wind ceases on day 4, the salinity signal propagates slowly towards the east. By contrast, the zonal velocity rapidly shifts from westward to eastward (becoming stronger towards the east).

The cross-stream velocity (Fig. 18c) is initially onshore during the storm. Note that the point being displayed in the figure is in the middle of the water column (see Fig. 16c), i.e. outside of the bottom and surface boundary layers. As the wind-forcing stops, the secondary flow becomes offshore and is strongest in the two-dimensional (eastern) regime. Such offshore flow is required above the onshore transport in the bottom boundary layer in order to balance mass, because there is no longer a northward flow in the surface Ekman layer. The offshore flow is largest when the westward jet is decelerating. However, once the eastward relaxation jet is established the secondary flow becomes (weakly) onshore again. This southward flow, emanating from the interior of the basin, feeds the relaxation jet.

It is difficult to compare directly the secondary flow found in the model to that observed in the data, in part because the signals are smaller than the along-topography flow (exacerbated by any discrepancies in defining the alongstream direction in the observations). Nonetheless, there are notable similarities. In particular, during the spin-down phase of the storm (stage 3, Fig. 12e), the

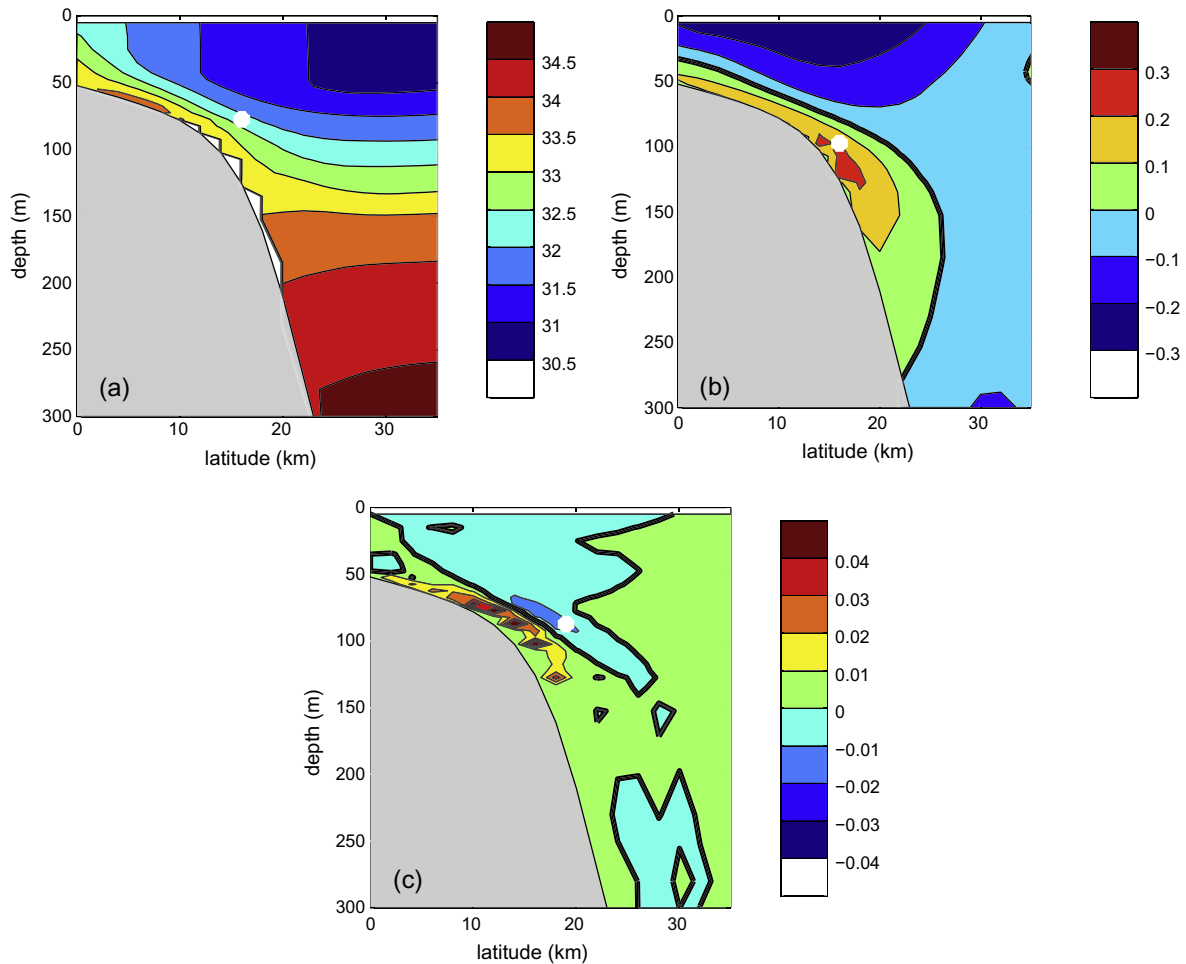


Fig. 17. Sections at 1500 km longitude on day 7 of (a) salinity (contour interval 0.5), (b) zonal velocity (contour interval 0.1 m s^{-1}), (c) meridional velocity (contour interval 0.01 m s^{-1}).

cross-stream flow in the Atlantic layer (where the relaxation jet ultimately appears) was directed offshore as the westward primary flow was decelerating. Following this, once the eastward relaxation jet was established, the observed cross-stream flow was onshore (stage 4, Fig. 12e). While not definitive, this is consistent with the magnitude and direction found in the model during the analogous phases of the storm. The main discrepancy is that the model does not produce the much stronger onshore flow measured in the shallower Pacific Water layer. It is possible that this observed feature results from a detail in the flow or the forcing, an instability, or a regional characteristic of the bottom topography.

4.2.4. Wave propagation

There are two key phase speeds that define the adjustment of the water column to the wind-forcing. The first is the barotropic shelf wave speed (the first mode), given approximately by $c_0 = fL(H - h_s)/H$, where L is the shelf width, H is the basin depth, and h_s is the average shelf depth (see Brink, 1982). For the present configuration of the Alaskan Beaufort shelf, $L = 25 \text{ km}$, $H = 450 \text{ m}$, and $h_s = 100 \text{ m}$. The resulting phase speed is 2.35 m s^{-1} and is marked in Fig. 18 by the two solid black lines. As one can see, a signal propagating at this speed closely matches the timing for which the salinity and velocity change from the two-dimensional to the three-dimensional solution moving from west to east (the direction of wave propagation) over the first four days of integration (the lower black line), consistent with the theory of Allen (1976). It is also the rate at which the zonal flow changes from westward

to eastward after the wind turns off (upper black line). A similar agreement between the predicted phase speed and the propagation speed diagnosed in the model is found for calculations in which the width of the shelf (L) is increased or decreased, so this interpretation is robust. We note that Aagaard and Roach (1990) deduced an eastward phase speed of 2.3 m s^{-1} for upwelling signals propagating along the Beaufort slope; this value, calculated using mooring records, is nearly identical to that calculated above. The sea surface height anomaly along the southern boundary is shown in Fig. 18d. The initial adjustment to wind-forcing shows decreasing sea surface height in response to the offshore Ekman transport, followed by a transition from the two-dimensional to the three-dimensional solution similar to that seen in salinity (lower black line). Once the wind-forcing has ceased, most of the sea surface height signal propagates rapidly towards the east—also at the barotropic shelf wave speed—similar to the alongstream velocity (upper black line). This qualitative behavior is insensitive to bottom drag because frictional spin-down of the barotropic component becomes important for length scales of $O(h_s c_0 / C_d) = 2350 \text{ km}$, which is larger than the length scale of the forcing and the relaxation jet region.

The second important phase speed is indicated by the black dashed line in Fig. 18. This is the phase speed for the third mode, $c = 0.41 \text{ m s}^{-1}$, which was found by solving the eigenvalue problem for the free waves given the ambient stratification and bottom topography, following the method outlined in Brink (2006). Note that after the wind is turned off the dominant salinity signal

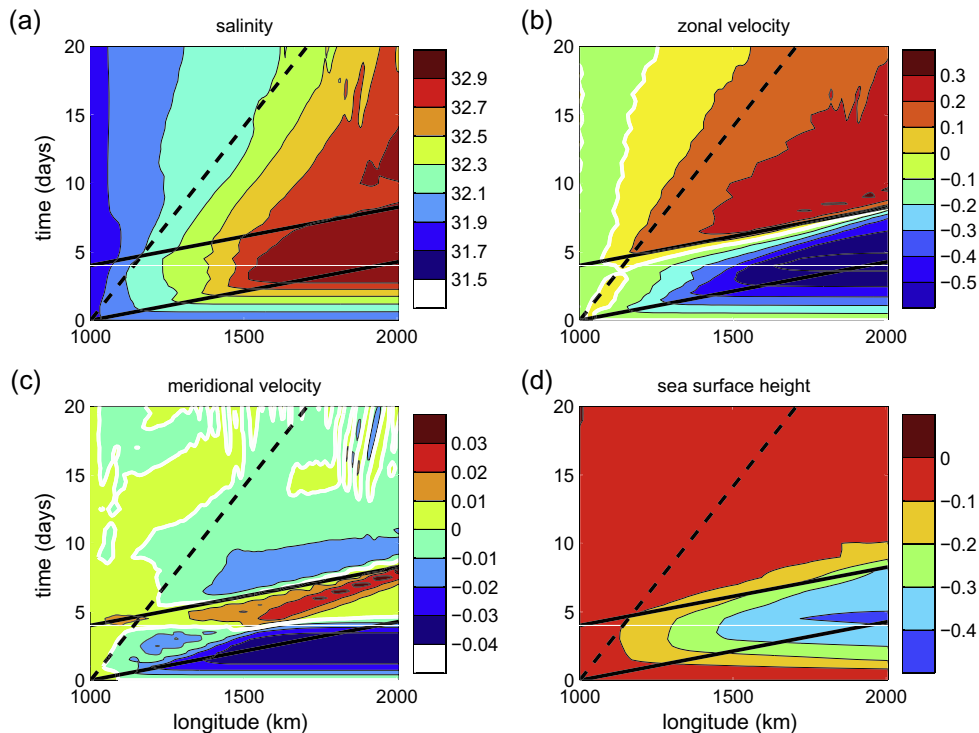


Fig. 18. Longitude–time plots of (a) salinity (contour interval 0.2), (b) zonal velocity (contour interval 0.1 m s^{-1}), (c) meridional velocity (contour interval 0.01 m s^{-1}), (d) sea surface height anomaly (contour interval 0.1 m). The locations of the time series are indicated by the white dots in Figs. 15–17. The sea surface height is at the southern boundary. The black solid line indicates a phase speed of 2.35 m s^{-1} (barotropic shelf wave); the black dashed line indicates a phase speed of 0.41 m s^{-1} (mode 3 wave). The thick white line in (b) and (c) is the zero line. The thin white line marks the time at which the wind-forcing is stopped.

propagates eastward at approximately this speed (Fig. 18a), while the sea surface height field shows no signal propagating this slowly (Fig. 18d). The second mode, which has a phase speed of 0.71 m s^{-1} , has a strong barotropic component over the shelf and so is not excited by the primarily baroclinic signal of the upwelled isopycnals.

These two time scales identify the key processes responsible for the set-up and relaxation of the velocity and salinity fields in response to the storm. In the absence of forcing, the velocity field will adjust to be in approximate geostrophic balance with the pressure field on the inertial time scale. The pressure field is determined by two components: the surface pressure, which is controlled by sea surface height, and the baroclinic pressure, which is controlled by the density field (here just the salinity field by construction). Once the wind stops, the now unbalanced sea surface height signal adjusts through a rapid barotropic wave response, as indicated in Fig. 18d. However, most of the salinity signal evolves on the slower baroclinic time scale, so to lowest order the baroclinic pressure gradient is unchanged over the shelf and upper slope shortly after the wind ceases. The velocity consequently adjusts to the rapid change in sea surface height while maintaining essentially the same thermal wind shear in the interior of the water column. The result is a weak westward current at the surface and an eastward flow—the relaxation jet—near the bottom (Fig. 17b).

Simulated Lagrangian trajectories produced from the model velocity fields indicate that water parcels follow very complex three-dimensional trajectories over the course of the storm. Parcels in the upper water column, roughly shallower than the shelfbreak, are advected several hundred km to the west. However, water parcels initially located within the depth range 100–200 m experience little net zonal displacement over the 20 day model integration. When the wind-forcing is active, this water is upwelled onto the shelf and carried westward, similar to what happens to the

shallower parcels. After the wind ceases, however, these waters downwell and are carried eastward in the relaxation jet, returning nearly to their original longitude.

Relaxation flow following wind events has been observed extensively along the northern and central California shelf. Following the cessation of upwelling-favorable northerly winds, a poleward current develops with associated warming of the water column (Send et al., 1987). Using 7 years of mooring data, Melton et al. (2009) demonstrated that the relaxation signals propagate northward at a speed of 10–30 km/day. A significant difference between this case and ours, however, is that the relaxation flow off of California is strongest on the inner-shelf (Winant et al., 1987), with virtually no signature of the current beyond the mid-shelf (Pringle and Dever, 2009). In contrast, the Beaufort Sea relaxation jet is maximum on the upper slope, extending as deep as 700 m (Nikolopoulos et al., 2009). There are also differences in how the jet is established. Similar to the Beaufort Sea, Pringle and Dever's (2009) model shows onshore flow feeding the relaxation flow for the California shelf. However, the adjustment of their poleward jet occurs on the (single) timescale of a low-mode coastal trapped wave. This is fundamentally different from our case where the disparate propagation speeds of the barotropic and baroclinic pressure fields dictate the establishment of the relaxation jet.

5. Chukchi sea response

It is of interest to consider the response of the November 2002 storm event over a wider geographical area, including the Chukchi Sea. In contrast to the Beaufort shelf, the Chukchi shelf is very wide, hence the continental slope is located far from the coast. As seen in Fig. 1, there a sharp bend in the orientation of the coastline at the northern-most tip of Alaska, and Barrow Canyon cuts

into the Chukchi shelf at this location. Consequently, it is not obvious what the wind-driven response will be to an Aleutian low storm over this broad area. While it is well-documented that upwelling occurs in Barrow Canyon during easterly wind events (e.g. Aagaard and Roach, 1990; Bourke and Paquette, 1976), the details of the response are unknown, including whether or not there is an upstream connection to the Chukchi shelfbreak. Here we take advantage of the fact that mooring data were collected at different sites in the Chukchi/Beaufort Seas during the November 2002 storm event (see Fig. 1), which provides a unique large-scale view. We begin first, however, by considering a regional scale application of the numerical model.

5.1. Regional model results

For the large-scale analysis the numerical model domain extends from 180°W to 140°W and 65°N to 77°N, with realistic bottom topography. The horizontal grid spacing is $1/30^\circ$ in both the zonal and meridional directions. The maximum depth in the model is 1300 m, with grid spacing varying from 5 m in the upper 115 m to 300 m near the bottom (a total of 30 levels). The initial stratification for temperature and salinity are horizontally uniform and taken from the November monthly mean PHC3.0 climatology (updated from Steele et al. 2001) at 152°W, 74°N. The salient model results are not sensitive to this initial stratification. Subgridscale mixing is parameterized with a Laplacian viscosity and diffusivity of $15 \text{ m}^2 \text{ s}^{-1}$. Vertical viscosity is $10^{-4} \text{ m}^2 \text{ s}^{-1}$, vertical diffusivity is $10^{-5} \text{ m}^2 \text{ s}^{-1}$, and a quadratic bottom drag of 10^{-3} is applied.

The model is spun-up from rest with the NCEP climatological mean October wind stress for a period of six months. The model does not explicitly include ice, although the reduction in wind speed found in the NCEP data does to some extent reflect the ice cover as discussed above. As will be shown, the key feature that drives the large-scale circulation during the storm event in question is the maximum in wind stress over the open ocean in the Chukchi Sea (see Fig. 5). Such a maximum will exist even if an ice model is considered, provided that the stress imparted on the ocean decays as one moves from the ice-free Chukchi Sea to the nearly 100% ice-covered interior (where internal ice stresses inhibit the movement of the ice). The model is also forced with a transport through Bering Strait, which is removed along the eastern boundary through a channel that connects back to Bering Strait from the south. A similar forcing was used by Spall (2007) and produced a realistic annual mean and seasonal cycle throughout the Chukchi Sea. Such a detailed analysis is not carried out here, however, as the primary reason for including this forcing is to develop an eastward flowing shelfbreak jet along the Beaufort Sea and northern Chukchi Sea as an initial state for the storm event.

The mean transport through Bering Strait at the end of the six month spin-up period is 0.6 Sv. This is less than the annual mean transport of approximately 0.8 Sv, but consistent with the October value of the monthly climatology for the Bering Strait through-flow established from 14 years of mooring data (1990–2004) by Woodgate et al. (2005b). The northward-flowing Pacific Water progresses across the Chukchi shelf through Herald Canyon, the Central Channel, and along the west coast of Alaska. In the model, nearly all of the transport ends up on the eastern side of Barrow Canyon and flows into the Alaskan Beaufort Sea. The sea surface height and horizontal velocities at several locations across the region at the end of this spin-up period are shown in Fig. 19b (these are the approximate locations of the moorings discussed below). The flow is northward through Central Channel, eastward along the northern Chukchi shelfbreak, northeast through Barrow Canyon, and eastward at 152°W on the Beaufort slope.

After the spin-up period, the flow through Bering Strait is maintained, and the surface winds from NCEP for the period November

1–11, 2002 are applied (for timing see Fig. 19a). The response at the peak of the storm is shown in Fig. 19c. Along the Beaufort slope the response is qualitatively similar to that recorded by the moorings and produced by the idealized calculation of the previous section. There is, however, a large scale adjustment in the Chukchi Sea that dominates the pre-existing circulation prior to the storm. Since the winds are northeasterly over the central Chukchi Sea (Fig. 5), this drives an offshore Ekman transport. Correspondingly, the sea surface height falls along the Alaskan coast (Fig. 19c). Recall, however, that the wind speed is significantly diminished seaward of the ice edge (Fig. 5), which means that the Ekman transport is greatly reduced there. This causes a convergence of the Ekman transport between the coastal region and the ice edge, which in turn increases the sea surface height over the northern Chukchi Sea (Fig. 19c). There is also an increase in sea surface height along the coast of Siberia caused by the northerly winds. The change in sea surface height from the Alaskan coast to the northern Chukchi Sea is substantial, exceeding 1 m.

The model velocity field adjusts to this variation in sea surface height arising from the curl of the windstress by developing an anti-cyclonic gyre over the northern Chukchi Sea and a smaller cyclonic gyre north of Bering Strait (Fig. 19c). The velocity at 152°W is westward during the storm, as expected for upwelling favorable winds. In contrast, the velocity along the northern Chukchi slope increases towards the east during the storm; i.e., the flow is upwind. The zonal velocity along the northern Chukchi Sea is more closely related to the time integral of the wind, not the wind strength itself. Hence, this flow is strongest subsequent to the peak of the storm. The flow in Central Channel also responds to the storm, reversing towards the southwest as a result of the anti-cyclonic gyre. In Barrow Canyon, coastal upwelling produces a strong southwestward flow along the eastern flank. The western flank of the canyon also develops a (weaker) southwestward flow during the storm, reflecting the return flow of the anti-cyclonic gyre (Fig. 19c).

At the end of the storm the model velocity along the Beaufort slope quickly returns to its original state of eastward flow, similar to what was produced by the idealized calculations and observed by the moorings (Fig. 19d). The same is true of the flow along the eastern side of Barrow Canyon, which promptly re-adjusts to flow towards the northeast. However, the circulation over the northern Chukchi shelf remains anti-cyclonic, with strong eastward flow along the shelfbreak, southward flow on the western side of Barrow Canyon, and westward flow in the Central Channel (Fig. 19d). These differences in post-storm adjustment can be explained as follows. As discussed above, the coastal region (including the east side of Barrow Canyon and the Beaufort slope) returns to its original state very quickly as a result of rapid wave propagation. Indeed, note how the negative sea surface height anomaly along the Alaskan boundary present at the height of the storm disappears by the end of the storm (compare Fig. 19c and d). In contrast, the anti-cyclonic and cyclonic gyres on the Chukchi shelf, while reduced in strength, are still present after the storm. This is because they are not driven by upwelling directly, but are a response to the local maximum in sea surface height resulting from the convergence of the offshore Ekman transport. The gyres do not intersect the coastal wave guide and, as a result, these interior features will decay on a longer viscous time scale (or may be altered by some subsequent external forcing such as winds or flow through Bering Strait).

The model results suggest then that the wind-driven response to the Aleutian low storm in early November 2002 differed markedly over the broad Chukchi Sea shelf versus the narrow Beaufort Sea shelf. In particular, (1) while the shelfbreak jet of the Beaufort Sea reversed to the west, the Chukchi shelfbreak jet intensified to the east—in opposition to the wind—with no associated upwelling;

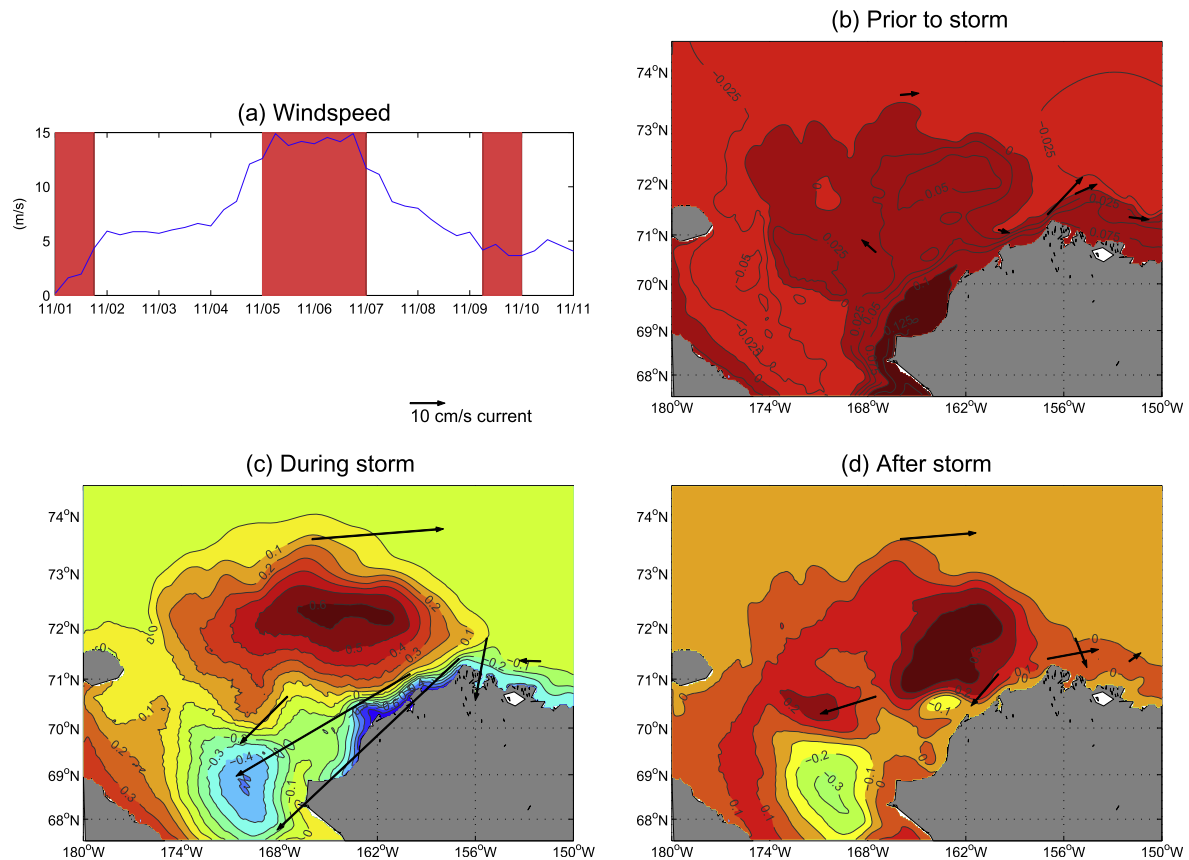


Fig. 19. Composite averages of the model currents and sea surface height during three periods of the storm. (a) Wind speed near Pt. Barrow from the NCEP reanalysis used in the model. The red denotes the periods of the three composite averages. (b) Composite average prior to the storm. The black vectors are the flow integrated over the depth of the water column, and the contours are sea surface height anomaly in meters (note that the contour interval is smaller than in the subsequent composites). (c) Composite average during the storm. (d) Composite average after the storm.

(2) there was significant up-canyon flow on both sides of Barrow Canyon during the storm; (3) the post-storm adjustment was rapid along the coast of Alaska (including the east side of Barrow Canyon and the Beaufort slope), but slow along the Chukchi slope, the western side of Barrow Canyon, and Central Channel. We now present moored velocity data that support these results.

5.2. Observations

As discussed in Section 2, in addition to the Beaufort slope moorings, the SBI program included mooring arrays on the Chukchi slope near 166°W, in Central Channel, and at the head of Barrow Canyon (see Fig. 1). Moorings were also maintained during this time period on both sides of the mouth of Barrow Canyon as part of a separate field program undertaken by JAMSTEC. Consequently, we were able to measure the response to the November 2002 storm event at a number of sites across the Chukchi and Beaufort Seas. Fig. 20 shows the timeseries of alongstream velocity and salinity in relation to the windspeed at each of the additional mooring sites for the first 12 days of November. The wind data are from NARR (blue curve), the salinity data are from point CTD measurements (red curve), and the velocity data (green curve) are from current meters or ADCPs (for the latter case only a single bin is displayed). See Table 1 for details, including the depths of the measurements. The dashed line in each plot corresponds to zero velocity.

Consider first the eastern side of Barrow Canyon. According to the model results the response at this site should be indicative of coastal upwelling. Fig. 20a suggests that this is the case. Prior to

the storm the flow is to the northeast (downcanyon) at $>50 \text{ cm s}^{-1}$. Similar to the Beaufort slope, the flow reverses shortly after the wind increases, followed by a sudden increase in salinity. The upcanyon flow reaches a maximum of 1 m s^{-1} and the salinity increases by more than 2 to 34.7, indicative of Atlantic Water. The response at the head of the canyon is similar (Fig. 20b), except that the Atlantic Water arrives about half a day later. As the winds subside, the upcanyon flow vanishes at both the head and mouth of the canyon, and the salinity drops (more so at the mouth).

The response along the Chukchi slope at 166°W is fundamentally different (Fig. 20c, where only the onshore mooring is displayed). After the easterly winds increase, the flow of the shelfbreak jet accelerates to the east. In addition, there is no evidence of upwelling of Atlantic Water; in fact, the salinity tends to decrease throughout the event (note the difference in salinity scale). Both of these features are consistent with the model and support the existence of the large anti-cyclonic gyre that is established in the model in the northern Chukchi Sea (Fig. 19c). Furthermore, note the difference in timing between the enhanced eastward flow observed along the Chukchi slope and the upcanyon flow in Barrow Canyon. The eastward flow peaks when the upcanyon flow has nearly vanished. This discrepancy is also consistent with the model, which indicates that the flow of the Chukchi shelfbreak jet responds to the time integral of the wind.

The observations indicate that the response to the storm was different on the two sides of the mouth of Barrow Canyon, as was the case in the model. While the flow was directed upcanyon on the western side of the canyon during the storm, as was true on the eastern flank, the speed was significantly weaker (50 cm s^{-1} vs.

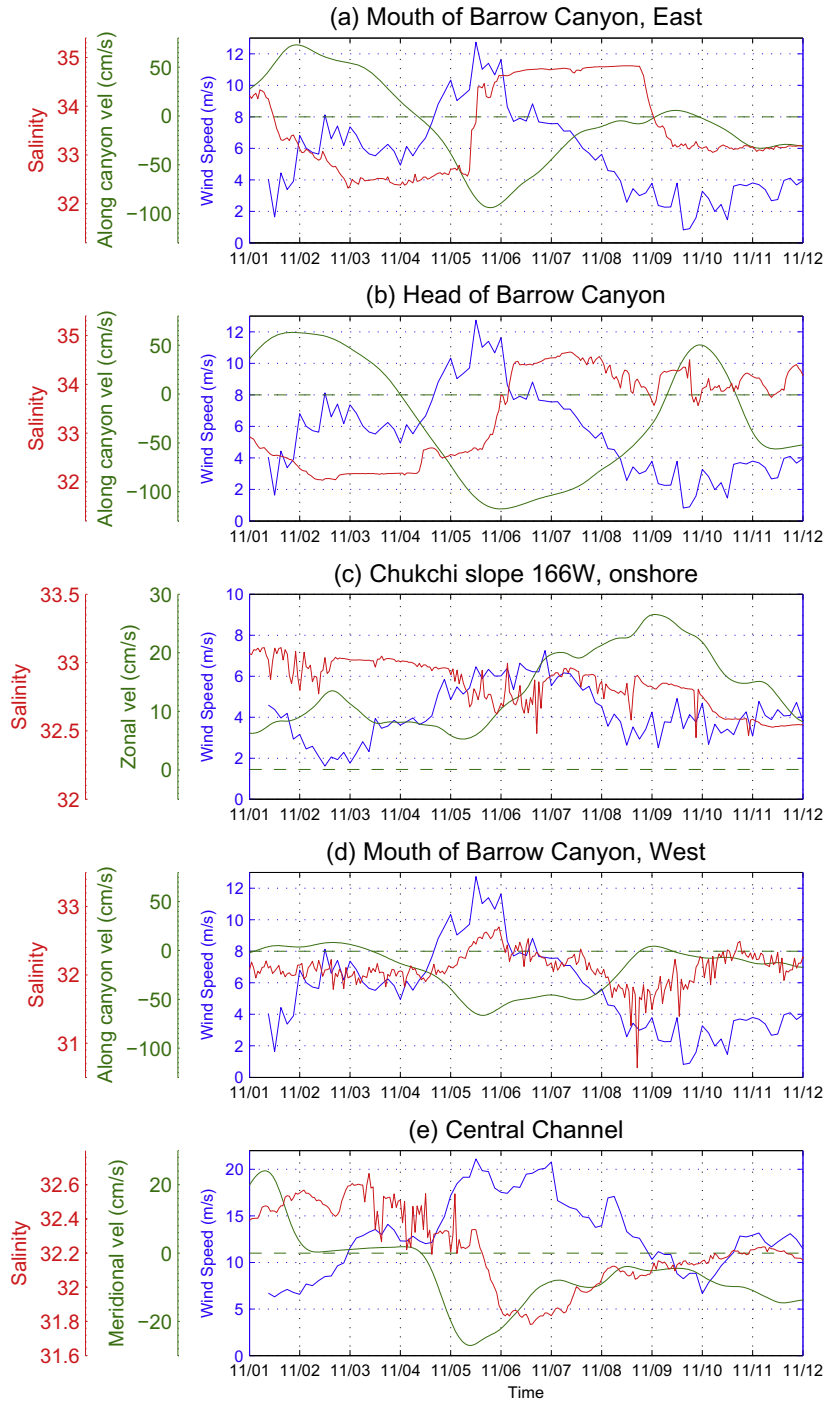


Fig. 20. Timeseries during the storm at the different mooring array sites. The velocity zero-crossing is indicated by the dashed line. See Table 1 for measurement depths.

Table 1
Additional mooring measurements used in the study.

Location	Latitude (N)	Longitude (W)	Depth of velocity (m)	Depth of salinity (m)	Rotation angle (°T)
Chukchi slope offshore	166°2.51'	73°36.68'	56	76	90
Chukchi slope onshore	166°3.59'	73°20.33'	56	61	90
Mouth of Barrow Canyon west	71°48.14'	155°19.86'	74	51	60
Mouth of Barrow Canyon east	71°40.29'	154°59.09'	71	86	60
Head of Barrow Canyon	71°3.09'	159°32.82'	65	67	60
Central Channel	70°40.39'	167°3.84'	43	33	0

100 cm s⁻¹, compare Fig. 20a and d). And while the salinity increased on the western side, the signal was small. In fact, Atlantic Water was not measured on this side of the canyon. Following Nikolopoulos et al. (2009) we take the salinity boundary between Pacific and Atlantic water to be 33.64, and the salinity only increased to 32.57 at this site. (It should be noted, however, that the depth of the salinity measurement at this mooring was less than on the eastern side (Table 1) which could have played a role in the reduced salinity signal.) The mooring in Central Channel also detected a storm response. As the winds increased the flow was directed to the south, and shortly thereafter the salinity experienced a sudden change. However, unlike Barrow Canyon, the salinity decreased at this site. This indicates that, during the storm, Atlantic Water did not appear in Central Channel, and suggests instead that fresher water resident on the northern Chukchi shelf was advected southward.

To highlight the regional differences measured by the moorings, and to allow for a more direct comparison to the model results, we have constructed the analogous flow vector composites that were shown earlier for the model (Fig. 19). These are shown for the data in Fig. 21. We note that the magnitude of the measured flow differs from that found in the model. However, we are most interested in comparing the general trends in the circulation over the evolution of the storm event. Prior to the storm there was strong outflow from Barrow Canyon, both at the canyon head and the eastern side of the canyon mouth (Fig. 21b). However, the outflow at the western side of the mouth was weak. This is not surprising since the undisturbed flow of the Chukchi shelfbreak jet should follow topographic contours into the western side of Barrow Canyon, meeting the canyon outflow there and perhaps causing some stagnation of the flow. Before the storm, the current was northward through Central Channel and eastward along the Chukchi slope.

At the height of the storm the flow had reversed throughout Barrow Canyon, as well as in Central Channel and along the Beaufort slope (Fig. 21c). Along the Chukchi slope, however, the flow became stronger to the east. These trends are in line with the model results. After the winds subsided, the alongstream flow was beginning to re-establish at the head of Barrow Canyon, the east side of Barrow Canyon, and along the Beaufort shelfbreak (Fig. 21d). Recall that these are sites influenced by the propagation of the fast coastal waves. In contrast, the eastward flow on the Chukchi slope remained strong after the storm and was still entering the west side of Barrow Canyon. The flow in Central Channel remained southward as well. According to the model, these three sites were influenced by the anti-cyclonic gyre that developed in the northern Chukchi Sea, whose spin-down was slow compared to the coastal sites. Overall then, the measured flow vectors displayed strong similarity to the model circulation throughout the storm, adding credence to the dynamical interpretations presented above.

5.3. Implications

As mentioned earlier, upwelling of warm and salty Atlantic Water is observed in Barrow Canyon. However, both Mountain et al. (1976) and Aagaard and Roach (1990) found little correlation between observed currents in the canyon and the local winds. This led Aagaard and Roach (1990) to investigate the role of remote forcing. Using moored records in Barrow Canyon (located at mid-canyon) and at two sites along the Beaufort slope (near 153°W and 147° W), they found evidence of lagged correlation in temperature, salinity, and velocity, leading them to conclude that upwelling signals were being carried eastward by shelf waves. Aagaard and Roach (1990) hypothesized that such signals originated from the west and subsequently propagated along the edge of the

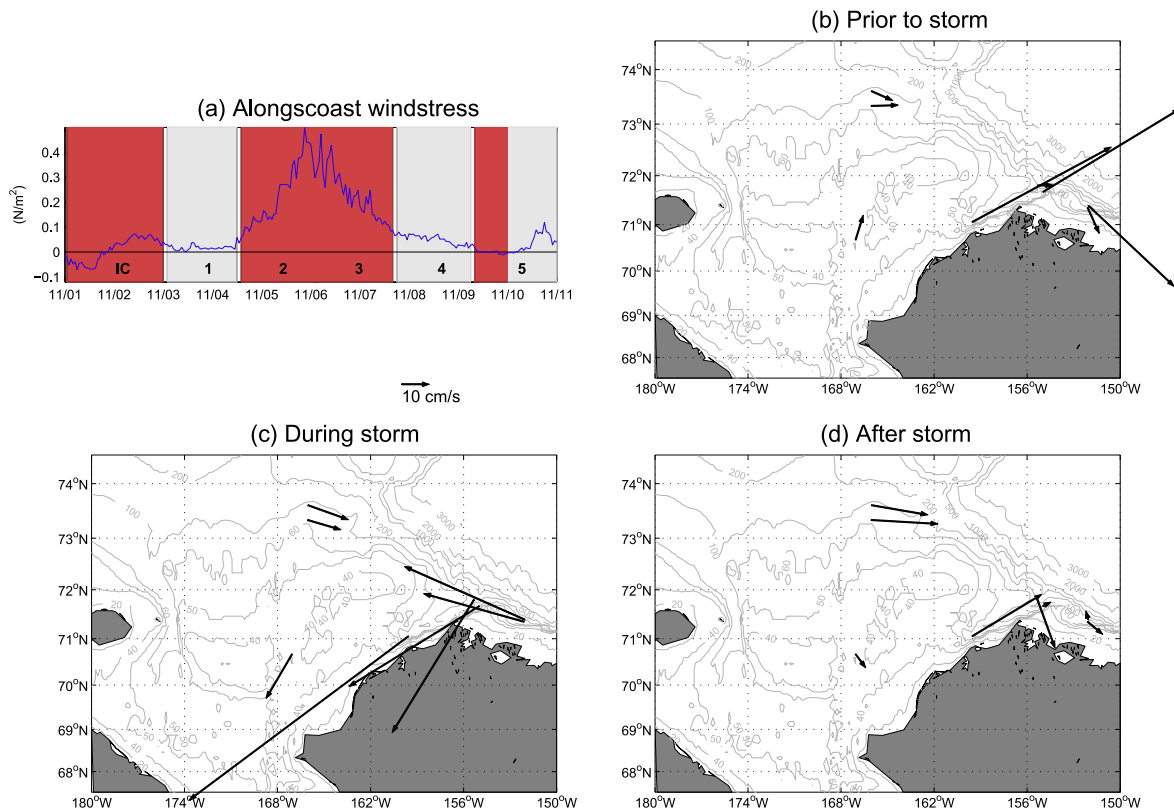


Fig. 21. Composite averages of the observed currents during three periods of the storm. (a) Alongcoast windstress at the Pt. Barrow meteorological station (positive stress corresponds to easterly winds). The five stages of the storm are marked in gray as in Fig. 9. The red denotes the periods of the three composite averages. (b) Composite average prior to the storm (stage “IC”). The vectors are the measured currents (see Table 1 for measurement depths). (c) Composite average during the storm (stages 2 and 3). (d) Composite average after the storm (first part of stage 5).

Chukchi shelf towards Barrow Canyon, driving the Atlantic Water up the canyon.

We have found that for the November 2002 storm event the upwelling was a mix of a local response modulated by the shelf wave signal. In our case the western edge of the storm, in the coastal sense, is in the region of Pt. Hope in the Chukchi Sea (Figs. 1 and 5), and signals did not propagate along the shelfbreak but along the west/north coast of Alaska. The farther east one progresses along the Alaskan coast into the Beaufort Sea, the more the response is dominated by local winds. Aagaard and Roach (1990) also speculated that, because of the small width of Barrow Canyon, the pressure signal of the shelf waves would drive flow up both sides of the canyon. Our results suggest that, while upcanyon flow did occur on both sides of the canyon during the storm event in question, upwelled water from the basin appeared predominantly on the eastern flank while the western flank was comprised mostly of water from the Chukchi shelfbreak jet. Hence the nature of the upcanyon flow was different on either side of the canyon.

One might ask how representative the November 2002 storm was. While the winds were especially strong, many of the storm's characteristics were typical of the canonical autumn Aleutian low (see Pickart et al., 2009a; Pickart et al., 2009b). Based on our model results, one of the governing factors in the broad-scale response is the location of the ice edge. Recall that the reduction in wind speed over the ice led to the establishment of the anti-cyclonic gyre and the enhanced eastward flow along the Chukchi slope. Model calculations in which the wind stress does not decrease offshore do not produce the anti-cyclone. Instead, weak cyclonic circulation dominates much of the Chukchi Sea. This implies that the large-scale response described here may only apply during the fall, i.e. as the ice edge encroaches on the Chukchi Sea.

There is evidence that this may be the case. Llinás et al. (2009) presented a summertime synoptic section across the Chukchi continental slope, occupied during an easterly wind event. Both the hydrographic fields and the velocity section were reminiscent of the post-storm adjustment phase described above for the Beaufort slope (see Fig. 4 of Llinás et al., 2009). In particular, the shelfbreak jet had a deep extension (to 250 m) advecting Atlantic Water to the east, while offshore of this there was surface-intensified westward flow. Furthermore, the Atlantic Water isopycnals were sloped upwards towards the continental slope. This scenario is very similar to stage 4 of the present storm (Fig. 13). Llinás et al.'s (2009) section was occupied in late August 2004 during an Aleutian low that was located in the same area as the storm analyzed here. However, the ice edge was located far to the north in the Canada Basin (near 78°N), and the winds decayed much more gradually in the meridional direction. In this case, without the anti-cyclonic gyre present, the response along the Chukchi shelfbreak might be more indicative of coastal upwelling (with a wide shelf). A similar three-dimensional solution would be expected—including the establishment of the post-storm deep relaxation flow—since the western edge of the storm is located in the vicinity of 180°W.

The implication is that the location of the ice edge could help dictate the presence or absence of upwelling along the Chukchi slope, and that Aleutian lows occurring in late-spring to early-fall may bring Atlantic water onto the Chukchi shelf. Keep in mind that the Aleutian low storm activity is in general strongest in the fall and winter (e.g. Favorite et al., 1976), so this implies that Barrow Canyon (in particular its eastern flank) will still be the most effective location for such wind-driven flow onto the shelf. However, in light of the recent trend of diminished pack-ice in the western Arctic (and a longer open water period), enhanced on-shelf fluxes of heat, salt, and nutrients may be occurring along the entire northern boundary of the Chukchi Sea. This requires further investigation, as does the overall role of sea ice (both pack-ice and land-fast ice) on upwelling in the Beaufort and Chukchi Seas.

Acknowledgments

The authors thank Steve Lentz and Ken Brink for helpful discussions during the course of the work. The following grants provided support for this study. National Science Foundation grants OPP-0731928 (RP and MS), OPP-0713250 (RP), OPP-0901407 and OPP-0908124 (RW); Office of Naval Research Grant N00014-02-1-0305 (KA), N00014-07-1-1040 (TW); Natural Sciences and Engineering Research Council of Canada (GWKM).

References

- Aagaard, K., 1984. The Beaufort Undercurrent. *The Alaskan Beaufort Sea: Ecosystems and Environments*. Academic Press. pp. 47–71.
- Aagaard, K., Roach, E., 1990. Arctic ocean-shelf exchange: measurements in Barrow Canyon. *Journal of Geophysical Research* 95, 18163–18175.
- Aagaard, K., Coachman, L., Carmack, E., 1981. On the halocline of the Arctic Ocean. *Deep Sea Research* 28, 529–545.
- Adcroft, A., Hill, C., Marshall, J., 1997. Representation of topography by shaved cells in a height coordinate ocean model. *Monthly Weather Review* 125, 2293–2315.
- Allen, J.S., 1976. Some aspects of the forced wave response of stratified coastal regions. *Journal of Physical Oceanography* 6, 113–119.
- Bourke, R.H., Paquette, R.G., 1976. Atlantic water on the Chukchi shelf. *Geophysical Research Letters* 3, 629–632.
- Brink, K.H., 1982. A comparison of long coastal trapped wave theory with observations off Peru. *Journal of Physical Oceanography* 12, 897–913.
- Brink, K.H., 2006. Coastal-trapped waves with finite bottom friction. *Dynamics of Atmospheres and Oceans* 41, 172–190.
- Carmack, E.C., Kulikov, E.A., 1998. Wind-forced upwelling and internal Kelvin wave generation in Mackenzie Canyon, Beaufort Sea. *Journal of Geophysical Research* 103, 18447–18458.
- Carmack, E., Wassmann, P., 2006. Food webs and physical–biological coupling on pan-Arctic shelves: unifying concepts and comprehensive perspectives. *Progress in Oceanography* 71, 446–477.
- Cavaliere, D.J., Martin, S., 1994. The contribution of Alaskan, Siberian, and Canadian coastal polynyas to the cold halocline layer of the Arctic Ocean. *Journal of Geophysical Research* 99, 18343–18362.
- Chao, S.-Y., Shaw, P.-T., 2003. Heteron shedding from submarine-canyon plumes in an Arctic boundary current system: sensitivity to the Undercurrent. *Journal of Physical Oceanography* 33, 2032–2044.
- Chapman, D.C., Carmack, E.C., 2003. Wind-driven shelf/basin exchange on an Arctic shelf: the joint roles of ice cover extent and shelfbreak variability. *Geophysical Research Letters* 30 (14), 1778. doi:10.1029/2003GL017526.
- Chu, P.C., 1987. An ice breeze mechanism for an ice divergence–convergence criterion in the marginal ice zone. *Journal of Physical Oceanography* 17, 1627–1632.
- Dickey, W.W., 1961. A study of a topographic effect on wind in the Arctic. *Journal of Meteorology* 18, 790–803.
- Doyle, J.D., Shapiro, M.A., 1999. Flow response to large-scale topography: the Greenland tip jet. *Tellus* 51, 728–748.
- Favorite, F., Dodimead, A.J., Nasu, K., 1976. Oceanography of the subarctic Pacific region, 1962–72. *Bulletin of the International North Pacific Commission* 33, 1–187.
- Hoskins, B.J., McIntyre, M.E., Robertson, A.W., 1985. On the use and significance of isentropic potential vorticity maps. *Quarterly Journal of the Royal Meteorological Society* 111, 877–946.
- Jones, E.P., Swift, J.H., Anderson, L.G., Lipizer, M., Civitarese, G., Falkner, K.K., Kattner, G., McLaughlin, F., 2003. Tracing Pacific water in the North Atlantic Ocean. *Journal of Geophysical Research* 108. doi:10.1029/2001JC001141.
- Large, W.G., Pond, S., 1981. Open ocean momentum flux measurements in moderate to strong winds. *Journal of Physical Oceanography* 11, 324–336.
- Lentz, S.J., 1987. A description of the 1981 and 1982 spring transitions over the northern California shelf. *Journal of Geophysical Research* 92, 1545–1567.
- Lentz, S.J., Chapman, D.C., 2004. The importance of non-linear cross-shelf momentum flux during wind-driven coastal upwelling. *Journal of Physical Oceanography* 34, 2444–2457.
- Llinás, L., Pickart, R.S., Mathis, J.T., Smith, S.L., 2009. Zooplankton inside an arctic cold-core eddy: probable origin and fate. *Deep Sea Research* 56, 1290–1304.
- Mahoney, A.H., Eicken, H., Gaylord, A.G., Shapiro, L., 2007. Alaska landfast sea ice: links with bathymetry and atmospheric circulation. *Journal of Geophysical Research* 112. doi:10.1029/2006JC003559x.
- Manley, T.O., Hunkins, K., 1985. Mesoscale eddies of the Arctic Ocean. *Journal of Geophysical Research* 90, 4911–4930.
- Marshall, J., Hill, C., Perelman, L., Adcroft, A., 1997. Hydrostatic, quasi-hydrostatic, and non-hydrostatic ocean modeling. *Journal of Geophysical Research* 102, 5733–5752.
- Mathis, J.T., Pickart, R.S., Hansell, D.A., Kadko, D., Bates, N.R., 2007. Eddy transport of organic carbon and nutrients from the Chukchi shelf into the deep Arctic basin. *Journal of Geophysical Research* 112. doi:10.1029/2006JC00389.
- Melling, H., 1993. The formation of a haline shelf front in wintertime in an ice-covered Arctic sea. *Continental Shelf Research* 13, 1123–1147.

- Melton, C., Washburn, L., Gotschalk, C., 2009. Wind relaxations and poleward flow events in a coastal upwelling system on the central California coast. *Journal of Geophysical Research* 114, C11016. doi:10.1029/2009JC005397.
- Mesinger, F., DiMego, G., Kalnay, E., Mitchell, K., Shafran, P.C., et al., 2006. North American regional reanalysis. *Bulletin of the American Meteorological Society* 87, 343–360.
- Moore, G.W.K., Renfrew, I.A., 2005. Tip jets and barrier winds: a QuikSCAT climatology of high wind speed events around Greenland. *Journal of Climate* 18, 3713–3725.
- Mountain, D.G., 1974. Bering Sea water on the north Alaskan shelf. Ph.D. Thesis, University of Washington, Seattle, WA, 153 pp.
- Mountain, D.G., Coachman, L.K., Aagaard, K., 1976. On the flow through Barrow Canyon. *Journal of Physical Oceanography* 6, 461–470.
- Muench, R.D., Gunn, J.T., Whittle, T.E., Schlosser, P., Smethie Jr., W., 2000. An Arctic cold core eddy. *Journal of Geophysical Research* 105, 23997–24006.
- Nelson, R.J., Carmack, E.C., McLaughlin, F.A., Cooper, G.A., 2009. Penetration of Pacific zooplankton into the western Arctic Ocean tracked with molecular population genetics. *Marine Ecology Progress Series* 381, 129–138.
- Nikolopoulos, A., Pickart, R.S., Fratantoni, P.S., Shimada, K., Torres, D.J., Jones, E.P., 2009. The western arctic boundary current at 152°W: structure, variability, and transport. *Deep Sea Research II* 56, 1164–1181.
- Pickart, R.S., Stossmeister, G., 2008. Outflow of Pacific water from the Chukchi sea to the Arctic Ocean. *Chinese Journal of Polar Oceanography* 10, 135–148.
- Pickart, R.S., Torres, D.J., Fratantoni, P.S., 2004. Shelfbreak circulation in the Alaskan Beaufort sea: mean structure and variability. *Journal of Geophysical Research* 109. doi:10.1029/2003JC001912.
- Pickart, R.S., Pratt, L.J., Zimmermann, S., Torres, D.J., 2005. Flow of winter-transformed water into the western Arctic. *Deep Sea Research II* 52, 3175–3198.
- Pickart, R.S., Våge, K., Moore, G.W.K., Renfrew, I.A., Ribergaard, M.H., Davies, H.C., 2008. Convection in the western North Atlantic sub-polar gyre: do small-scale wind events matter? In: Dickson, R.R., Meincke, J., Rhines, P. (Eds.), *Arctic-Subarctic Ocean Fluxes: Defining the Role of the Northern Seas in Climate*. Springer, pp. 629–652.
- Pickart, R.S., Moore, G.W.K., Macdonald, A.M., Renfrew, I.A., Walsh, J.E., Kessler, W.S., 2009a. Seasonal evolution of Aleutian low-pressure systems: implications for the North Pacific sub-polar circulation. *Journal of Physical Oceanography* 39, 1316–1339.
- Pickart, R.S., Moore, G.W.K., Torres, D.J., Fratantoni, P.S., Goldsmith, R.A., Yang, J., 2009b. Upwelling on the continental slope of the Alaskan Beaufort Sea: storms, ice, and oceanographic response. *Journal of Geophysical Research* 114, C00A13. doi:10.1029/2208JC005009.
- Pringle, J.M., Dever, E.P., 2009. Dynamics of wind-driven upwelling and relaxation between Monterey Bay and Point Arena: local-, regional-, and gyre-scale controls. *Journal of Geophysical Research* 114, C07003. doi:10.1029/2008JC005016.
- Send, W., Beardsley, R.C., Winant, C.D., 1987. Relaxation from upwelling in the Coastal Ocean Dynamics experiment. *Journal of Geophysical Research* 92, 1683–1698.
- Shimada, K., Itoh, M., Nishino, S., McLaughlin, F., Carmack, E., Proshutinsky, A., 2005. Halocline structure in the Canada Basin of the Arctic Ocean. *Geophysical Research Letters* 32, L0360. doi:10.1029/2004GL021358.
- Shimada, K., Kamoshida, T., Itoh, M., Nishino, S., Carmack, E., McLaughlin, F., Zimmermann, S., Proshutinsky, A., 2006. Pacific Ocean inflow: influence on catastrophic reduction of sea ice cover in the Arctic Ocean. *Geophysical Research Letters* 33, L08605. doi:10.1029/2005GL025624.
- Skamarock, W.C., Klemp, J.B., 2008. A time-split nonhydrostatic atmospheric model for weather research and forecasting applications. *Journal of Computational Physics* 227, 3465–3485.
- Smagorinsky, J., 1963. General circulation experiments with the primitive equations: I. The basic experiment. *Monthly Weather Review* 91, 99–164.
- Spall, M.A., 2007. Circulation and water mass transformation in a model of the Chukchi Sea. *Journal of Geophysical Research* 112, C05025. doi:10.1029/2005JC003364.
- Spall, M.A., Pickart, R.S., Fratantoni, P.S., Plueddemann, A.J., 2008. Western arctic shelfbreak eddies: formation and transport. *Journal of Physical Oceanography* 38, 1644–1668.
- Våge, K., Spengler, T., Davies, H.C., Pickart, R.S., 2009. Multi-event analysis of the westerly Greenland tip jet based upon 45 winters in ERA-40. *Quarterly Journal of the Royal Meteorological Society* 135, 1999–2011.
- von Appen, W.-J., Pickart, R.S., 2010. Two configurations of the western Arctic shelfbreak jet advecting Pacific summer water in the Alaskan Beaufort Sea. In: *EOS Trans. AGU, 91. Ocean Sci. Meet. Suppl. (Abstract P034C-05)*.
- Walsh, J.J. et al., 1989. Carbon and nitrogen cycling within the Bering/Chukchi Seas: source regions for organic matter effecting AOU demands of the Arctic Ocean. *Progress in Oceanography* 22, 277–259.
- Watanabe, E., Hasumi, H., 2009. Pacific water transport in the western Arctic ocean simulated by an eddy-resolving coupled ice-ocean model. *Journal of Physical Oceanography* 39, 2194–2211.
- Williams, W.J., nd Carmack, E.C., 2010. The effect of retreating summer ice on shelf-break exchange in the Arctic Ocean. In: *EOS Trans. AGU, 91. Ocean Sci. Meet. Suppl. (Abstract IT15G-04)*.
- Williams, W.J., Melling, H., Carmack, E.C., Ingram, R.G., 2008. Kugmallit Valley as a conduit for cross-shelf exchange on the Mackenzie shelf in the Beaufort Sea. *Journal of Geophysical Research* 113. doi:10.1020/2006JC003591.
- Wilson, J.G., Overland, J.E., 1986. *Meteorology*. In: Hood, D.W., Zimmermann, S.T. (Eds.), *The Gulf of Alaska, Physical Environment and Biological Resources*. Alaska Office, Ocean Assessments Division, National Oceanic and Atmospheric Administration, US Department of Commerce, pp. 31–54.
- Winant, C., Beardsley, R., Davis, R., 1987. Moored wind, temperature, and current observations made during coastal ocean dynamics experiments 1 and 2 over the northern California continental shelf and upper slope. *Journal of Geophysical Research* 92, 1569–1604.
- Woodgate, R.A. et al., 2004. Cruise report for the USCGC Healy HLY-03-03 SBI mooring cruise, September–October 2003. *Geophysical Research Letters* 33, L15609. doi:10.1029/2006GL026931.
- Woodgate, R.A., Aagaard, K., Swift, J.H., Falkner, K.K., Smethie, J.W.M., 2005a. Pacific ventilation of the Arctic Ocean's lower halocline by upwelling and diapycnal mixing over the continental margin. *Geophysical Research Letters* 32, L18609. doi:10.1029/2005GL023999.
- Woodgate, R.A., Aagaard, K., Weingartner, T.J., 2005b. A year in the physical oceanography of the Chukchi Sea: moored measurements from autumn 1990–1991. *Deep Sea Research II* 52, 3116–3149.
- Woodgate, R.A., Aagaard, K., Weingartner, T.J., 2006. Interannual changes in the Bering Strait fluxes of volume, heat and freshwater between 1991 and 2004. *Geophysical Research Letters* 33, L15609. doi:10.1029/2006GL026931.
- Woodgate, R.A., Weingartner, T.J., Lindsay, R., 2010. The 2007 Bering Strait oceanic heat flux and anomalous Arctic sea-ice retreat. *Geophysical Research Letters* 37. doi:10.1029/2009GL041621.
- Yang, J., 2006. The seasonal variability of the Arctic ocean Ekman transport and its role in the mixed layer heat and salt fluxes. *Journal of Climate* 19, 5366–5387.
- Zhang, J., Steele, M., Woodgate, R., 2008. The role of Pacific water in the dramatic retreat of Arctic sea ice during summer 2007. *Chinese Journal of Polar Oceanography* 19, 93–107.